

# 1 Large scale multi-layer fuel load characterization in 2 tropical savanna using GEDI spaceborne lidar data

3  
4 Rodrigo Vieira Leite<sup>1\*</sup>, Carlos Alberto Silva<sup>2</sup>, Eben North Broadbent<sup>3</sup>, Cibele Hummel  
5 do Amaral<sup>1</sup>, Veraldo Liesenberg<sup>4</sup>, Danilo Roberti Alves de Almeida<sup>5</sup>, Midhun  
6 Mohan<sup>6</sup>, Sérgio Godinho<sup>7,8</sup>, Adrian Cardil<sup>9,10,11</sup>, Caio Hamamura<sup>12</sup>, Bruno Lopes de  
7 Faria<sup>13</sup>, Pedro H. S. Brancalion<sup>5</sup>, André Hirsch<sup>14</sup>, Gustavo Eduardo Marcatti<sup>14</sup>, Ana  
8 Paula Dalla Corte<sup>15</sup>, Angelica Maria Almeyda Zambrano<sup>16</sup>, Máira Beatriz Teixeira da  
9 Costa<sup>17</sup>, Eraldo Aparecido Trondoli Matricardi<sup>17</sup>, Anne Laura da Silva<sup>14</sup>, Lucas  
10 Ruggeri Ré Y Goya<sup>14</sup>, Ruben Valbuena<sup>18</sup>, Bruno Araujo Furtado de Mendonça<sup>19</sup>, Celso  
11 H. L. Silva Junior<sup>20,21</sup>, Luiz E. O. C. Aragão<sup>20,22</sup>, Mariano García<sup>23</sup>, Jingjing Liang<sup>24</sup>,  
12 Trina Merrick<sup>25,26</sup>, Andrew T. Hudak<sup>27</sup>, Jingfeng Xiao<sup>28</sup>, Steven Hancock<sup>29</sup>, Laura  
13 Duncason<sup>30</sup>, Matheus Pinheiro Ferreira<sup>31</sup>, Denis Valle<sup>32</sup>, Sassan Saatchi<sup>33</sup>, Carine  
14 Klauberg<sup>15</sup>

15 <sup>1</sup>Department of Forest Engineering, Federal University of Viçosa (UFV), Av. Peter Henry  
16 Rolfs, 36570-900, Viçosa, MG, Brazil; [chamaral@ufv.br](mailto:chamaral@ufv.br), [rodrigo.leite@ufv.br](mailto:rodrigo.leite@ufv.br)

17 <sup>2</sup>Forest Biometrics and Remote Sensing Laboratory (Silva Lab), School of Forest, Fisheries,  
18 and Geomatics Sciences, University of Florida, University of Florida, PO Box 110410  
19 Gainesville, FL 32611; [c.silva@ufl.edu](mailto:c.silva@ufl.edu)

20 <sup>3</sup>Spatial Ecology and Conservation (SPEC) Lab, School of Forest, Fisheries, and Geomatics  
21 Sciences, University of Florida, Gainesville, FL 32611 USA; [eben@ufl.edu](mailto:eben@ufl.edu)

22 <sup>4</sup>Department of Forest Engineering, College of Agriculture and Veterinary, Santa Catarina  
23 State University (UDESC), Lages, SC, Brazil; [veraldo.liesenberg@udesc.br](mailto:veraldo.liesenberg@udesc.br)

24 <sup>5</sup>Department of Forest Sciences, “Luiz de Queiroz” College of Agriculture, University of São  
25 Paulo (USP/ESALQ), Piracicaba, SP, Brazil; [daniloraa@usp.br](mailto:daniloraa@usp.br); [pedrob@usp.br](mailto:pedrob@usp.br)

26 <sup>6</sup>Department of Geography, University of California—Berkeley, Berkeley, CA 94709, USA;  
27 [mid\\_mohan@berkeley.edu](mailto:mid_mohan@berkeley.edu)

28 <sup>7</sup>EaRSLab—Earth Remote Sensing Laboratory, University of Évora, 7000-671 Évora, Portugal

29 <sup>8</sup>Institute of Earth Sciences (ICT), Universidade de Évora, Rua Romão Ramalho, 59, 7002-554,  
30 Évora, Portugal; [sgodinho@uevora.pt](mailto:sgodinho@uevora.pt)

31 <sup>9</sup>Technosylva Inc, La Jolla, CA, USA, [adriancardil@gmail.com](mailto:adriancardil@gmail.com)

32 <sup>10</sup>Department of Crop and Forest Sciences, University of Lleida, Lleida, Spain

33 <sup>11</sup>Joint Research Unit CTFC - AGROTECNIO, Solsona, Spain

34 <sup>12</sup>Federal Institute of Education, Science and Technology of São Paulo, SP, 11533-160, Brazil;  
35 [hamamura.caio@ifsp.edu.br](mailto:hamamura.caio@ifsp.edu.br)

36 <sup>13</sup>Department of Forest Science, Federal University of Vales do Jequitinhonha e Mucuri,  
37 (UFVJM) Campus JK, Diamantina, MG, Brazil, [blfaria@gmail.com](mailto:blfaria@gmail.com)

38 <sup>14</sup>Federal University of São João Del Rei – UFSJ, Sete Lagoas, MG, Brazil, 35701-970;  
39 [hirsch\\_andre@ufsj.edu.br](mailto:hirsch_andre@ufsj.edu.br); [gustavomarcatti@ufsj.edu.br](mailto:gustavomarcatti@ufsj.edu.br); [annelsilva11@gmail.com](mailto:annelsilva11@gmail.com),  
40 [lucasgoya42.lr@gmail.com](mailto:lucasgoya42.lr@gmail.com), [carine\\_klauberg@hotmail.com](mailto:carine_klauberg@hotmail.com)

41 <sup>15</sup>Department of Forest Engineering, Federal University of Paraná (UFPR), Curitiba, PR,  
42 Brazil, 80.210-130; [anacorte@ufpr.br](mailto:anacorte@ufpr.br)

43 <sup>16</sup>Spatial Ecology and Conservation (SPEC) Lab, Center for Latin American Studies,  
44 University of Florida, Gainesville, FL 32611 USA; [aalmeyda@ufl.edu](mailto:aalmeyda@ufl.edu)

45 <sup>17</sup>Department of Forestry, University of Brasília, Campus Darcy Ribeiro, Brasilia, DF, Brazil -  
46 70.910-900; [mairabeatrizteixeira@hotmail.com](mailto:mairabeatrizteixeira@hotmail.com) ; [ematricardi@gmail.com](mailto:ematricardi@gmail.com)

47 <sup>18</sup>School of Natural Sciences, Bangor University, Bangor LL57 2W, UK.  
48 [r.valbuena@bangor.ac.uk](mailto:r.valbuena@bangor.ac.uk)

49 <sup>19</sup>Silviculture Department, Universidade Federal Rural do Rio de Janeiro, Rua da Floresta,  
50 Seropédica, RJ, 23897-005, Brazil; [brunomendonca@ufrj.br](mailto:brunomendonca@ufrj.br)

51 <sup>20</sup>National Institute for Space Research, Earth Observation and Geoinformatics Division, Av.  
52 dos Astronautas, 1758, São José dos Campos SP 12227-010, Brazil, [celsohlsj@gmail.com](mailto:celsohlsj@gmail.com),  
53 [luiz.aragao@inpe.br](mailto:luiz.aragao@inpe.br)

54 <sup>21</sup>Universidade Estadual do Maranhão (UEMA), Departamento de Engenharia Agrícola, São  
55 Luís, MA, 65055-310, Brazil

56 <sup>22</sup>College of Life and Environmental Sciences, University of Exeter, Exeter, UK

57 <sup>23</sup>Environmental Remote Sensing Research Group, Department of Geology, Geography and  
58 the Environment, Universidad de Alcalá, Calle Colegios 2, Alcalá de Henares, 28801, Spain.  
59 [mariano.garcia@uah.es](mailto:mariano.garcia@uah.es)

60 <sup>24</sup>Department of Forestry and Natural Resources, Purdue University, West Lafayette, IN,  
61 USA, [alpenbering@gmail.com](mailto:alpenbering@gmail.com)

62 <sup>25</sup>Department of Earth and Environmental Science, Vanderbilt University, Nashville, TN  
63 37240, USA

64 <sup>26</sup>Department of Geography, Florida State University, Tallahassee, FL, USA.  
65 [tmerrick@fsu.edu](mailto:tmerrick@fsu.edu)

66 <sup>27</sup>US Department of Agriculture, Forest Service, Rocky Mountain Research Station, 1221  
67 South Main Street, Moscow, ID 83843, USA, [andrew.hudak@usda.gov](mailto:andrew.hudak@usda.gov)

68 <sup>28</sup>Earth Systems Research Center, Institute for the Study of Earth, Oceans, and Space,  
69 University of New Hampshire, Durham, NH 03820, USA. [j.xiao@unh.edu](mailto:j.xiao@unh.edu)

70 <sup>29</sup>School of GeoSciences, University of Edinburgh, United Kingdom of Great Britain and  
71 Northern Ireland. [steven.hancock@ed.ac.uk](mailto:steven.hancock@ed.ac.uk)

72 <sup>30</sup> Department of Geographical Sciences, University of Maryland, College Park, MD 20740,  
73 USA; [lduncans@umd.edu](mailto:lduncans@umd.edu)

74 <sup>31</sup>Cartographic Engineering Section, Military Institute of Engineering (IME), Praça Gen.  
75 Tibúrcio 80, 22290-270 Rio de Janeiro-RJ, Brazil. [matheus@ime.eb.br](mailto:matheus@ime.eb.br)

76 <sup>32</sup> School of Forest, Fisheries, and Geomatics Sciences, University of Florida, PO Box 110410,  
77 136 Newins-Ziegler Hall, Gainesville, FL 32611; drvalle@ufl.edu

78 <sup>33</sup>NASA-Jet Propulsion Laboratory, California Institute of Technology, Pasadena, CA 91109,  
79 USA [sasan.s.saatchi@jpl.nasa.gov](mailto:sasan.s.saatchi@jpl.nasa.gov)

80  
81

82 \*Corresponding author: Tel: + 55 (31) 99229-7126; Email: [rodrigo.leite@ufv.br](mailto:rodrigo.leite@ufv.br)

83

84 **Abstract:**

85

86 Quantifying fuel load over large areas is essential to support integrated fire  
87 management initiatives in fire-prone regions to preserve carbon stock, biodiversity  
88 and ecosystem functioning. It also allows a better understanding of global climate  
89 regulation as a potential carbon sink or source. Large area assessments usually  
90 require data from spaceborne remote sensors, but most of them cannot measure the  
91 vertical variability of vegetation structure, which is required for accurately  
92 measuring fuel loads and defining management interventions. The recently launched  
93 NASA's Global Ecosystem Dynamics Investigation (GEDI) full-waveform lidar  
94 sensor holds potential to meet this demand. However, its capability for estimating  
95 fuel load has yet not been evaluated. In this study, we developed a novel framework  
96 and tested machine learning models for predicting multi-layer fuel load in the  
97 Brazilian tropical savanna (i.e., Cerrado biome) using GEDI data. First, lidar data  
98 were collected using an unnamed aerial vehicle (UAV). The flights were conducted,  
99 over selected sample plots in distinct Cerrado vegetation formations (i.e., grassland,  
100 savanna, forest) where field measurements were conducted to determine the load of  
101 surface, herbaceous, shrubs and small trees, woody fuels and the total fuel load.  
102 Subsequently, GEDI-like full-waveforms were simulated from the high-density  
103 UAV-lidar 3-D point clouds from which vegetation structure metrics were calculated  
104 and correlated to field-derived fuel load components using Random Forest models.  
105 From these models, we generate fuel load maps for the entire Cerrado using all on-  
106 orbit available GEDI data. Overall, the models had better performance for woody  
107 fuels and total fuel loads ( $R^2 = 0.88$  and  $0.71$ , respectively). For components at the  
108 lower stratum, models had moderate to low performance ( $R^2$  between  $0.15$  and  $0.46$ )  
109 but still showed reliable results. The presented framework can be extended to other  
110 fire-prone regions where accurate measurements of fuel components are needed. We  
111 hope this study will contribute to the expansion of spaceborne lidar applications for  
112 integrated fire management activities and supporting carbon monitoring initiatives  
113 in tropical savannas worldwide.

114

115 **Keywords:** Active remote sensing, fire, modeling, machine learning, UAV-lidar,  
116 Cerrado, vegetation structure

117

118  
119

## 120 1. Introduction

121 Climate change mitigation and biodiversity conservation efforts across the world  
122 require an understanding of wildfire dynamics (Bowman et al., 2013, Lehmann et al.  
123 2014). Tropical Savanna ecosystems are generally fire-adapted (Simon et al., 2009,  
124 Hoffmann et al., 2012, Durigan & Ratter, 2016), but human activities have affected  
125 fire regimes and landscape characteristics (Hantson et al., 2015, Andela et al., 2017,  
126 Andela et al., 2018, Rosan et al. 2019, Durigan et al. 2020). Fire dynamics in tropical  
127 savannas depend, among other factors, on the vegetation structure and accumulated  
128 fuel loads (combustible contents) (Sandberg et al., 2001, Chuvieco et al., 2003, Keane  
129 et al., 2013). Fuel load structure continuity, condition (live or dead) and moisture are  
130 important variables for modeling fire behavior (Stavros et al., 2018, Gomes et al.,  
131 2020a), assessing its severity (Hu et al. 2019, Klauberg et al., 2019), calculating  
132 greenhouse gas emissions (GHG) (Ogle et al., 2019, Gomes et al., 2020a) and  
133 improving landscape management and conservation strategies to promote a pyro-  
134 diverse ecosystem (Schmidt et al., 2018, Franke et al., 2018). These applications  
135 demand measurements of all fuel components as they interact with fire differently.  
136 That includes necromass (e.g., duff, litter, downed wood debris) and different plant  
137 types (e.g., grasses, herbs, forbs, shrubs, trees).

138 Remote sensing technologies are commonly used to examine fuel load  
139 distribution and spatial variability over large areas. In this regard, lidar (light

140 detection and ranging) sensors are preferred as they can directly detect different  
141 vegetation strata with high accuracy (Erdody et al., 2010, Gajardo et al., 2014,  
142 Szpakowski and Jensen 2019, Chuvieco et al., 2020). Generally, the approach for local  
143 scale fuel mapping relies on discrete-return or full-waveform lidar sensors in aircraft  
144 or unnamed aerial vehicle (UAV) platforms to collect lidar data and calculate lidar-  
145 derived metrics that will subsequently serve as predictor variables in statistical  
146 models (Hermosilla et al., 2014, Hudak et al., 2016a, Bright et al., 2017, Stefanidou et  
147 al., 2020). Nonetheless, when there are limited resources for airborne and UAV-lidar  
148 surveys, or it is necessary to upscale analyses to a regional/global level, images  
149 acquired by satellite systems operating in either optical or microwave domain are  
150 then required (Wulder et al., 2012, Garcia et al., 2017, Franke et al., 2018). The  
151 Geoscience Laser Altimeter System (GLAS, onboard ICESat-1 – Zwally et al., 2002)  
152 was the first spaceborne lidar sensor to collect sample data globally, and it was  
153 operational between 2003 and 2009. Although its main objective was to measure ice-  
154 sheet changes, GLAS was also used for forest and fuel-related studies (Lefsky et al.,  
155 2006, Duncanson et al., 2010, Ashworth et al., 2010, García et al., 2012, Peterson et al.,  
156 2013, Ferreira et al. 2011). Its successor mission launched in 2018, ICESat-2, is a  
157 photon-counting lidar system that also provides valuable 3-D sample data globally  
158 that can be similarly used for biomass estimation (Narine et al., 2020). Yet, neither of  
159 these missions' characteristics were optimized for collecting data over the global  
160 range of forest canopy structures which limits opportunities to use these data to  
161 examine some important biomes at regional scale.

162 A new promising near-global dataset for fuel load estimation comes from the  
163 Global Ecosystem Dynamics Investigation (GEDI) sensor, with unprecedented high  
164 resolution lidar data samples collected between  $\sim 52^\circ$  north and south latitudes,  
165 available since April 2019 (Dubayah et al., 2020a). As the first of its kind, GEDI was  
166 specifically designed to measure forest structure. The sensor is characterized as a  
167 large-footprint (diameter of  $\sim 25$  m) full-waveform lidar with penetration capability in  
168 forests with up to  $\sim 99\%$  canopy cover (Hancock et al., 2019, Duncanson et al., 2020).  
169 GEDI's penetration capabilities in dense vegetation is what mainly differentiates it  
170 from the previous spaceborne lidar sensors designed for ice sheet measurements.  
171 Furthermore, the footprints are separated at 60 m along track and 600 m across track  
172 - an improvement to GLAS' 70 m footprint separated  $\sim 170$  m along track (Zwally et  
173 al. 2002). The improved technical specification makes GEDI more suitable than any  
174 previous spaceborne sensor to measure forest structure at regional and global scales.

175 The GEDI mission plan includes the delivery of a global aboveground dry  
176 biomass (AGB) product at a spatial resolution of 1-km (Dubayah et al. 2020a) that is  
177 suitable for global biomass mapping requirements (Hall et al., 2011). These AGB  
178 estimates are expected to be the global benchmark of forest AGB, essential for  
179 measuring the world's carbon stocks. Furthermore, recent studies used GEDI  
180 waveform metrics for developing models to estimate forest height (Potapov et al.,  
181 2021, Rishmawi et al., 2021), biomass (Saarela et al., 2018, Silva et al., 2021,  
182 Duncanson et al., 2020, Rishmawi et al., 2021), and canopy structure diversity

183 ([Marselis et al., 2018](#), [Schneider et al., 2020](#), [Rishmawi et al., 2021](#)). However, to date,  
184 no published study on estimation of fuel loads from GEDI data is available and the  
185 GEDI AGB products may be of limited use for fire-related applications because  
186 calibration data to derive information on important layers may be lacking – such as  
187 from duff, litter, down woody debris, grasses, forbs and shrubs. In addition, these  
188 lower fuel strata layers that are crucial for fire behavior and emissions are commonly  
189 not considered in previous studies using spaceborne lidar sensors ([Lefsky et al. 2005](#),  
190 [Garcia et al. 2012](#), [Peterson et al. 2013](#)). Therefore, it is necessary to develop models  
191 using GEDI-derived metrics that consider all fuel load components for effectively  
192 meeting integrated fire management criteria and for improving carbon budget  
193 estimates.

194 Confirming GEDI's capability to predict fuel loads in savannas will open a range  
195 of new opportunities to improve fire management planning and decisions at regional  
196 and global scales. Furthermore, the possibility of having this information from space  
197 also opens the range of GEDI applications to map fuel loads during the mission life-  
198 span and for upcoming lidar satellite missions (e.g., Multi-footprint Observation  
199 Lidar and Imager - MOLI ([Murooka et al., 2013](#), [Kimura et al., 2017](#), [Asai et al., 2018](#))).  
200 The applications of such technological advances include mapping fire risk, carbon  
201 emissions and estimate fire behavior and fuel load dynamics for larger areas such as  
202 countries or entire biomes, thus contributing to mitigate the impacts of climate  
203 change in these regions. The overall aim of this study was to assess the capability of

204 GEDI for estimating large-scale multi-layer fuel loads in the Brazilian tropical  
205 savanna (Cerrado). Herein, we developed a framework to i) calibrate and validate  
206 Random Forest (RF) models for predicting different fuel layers (ground, surface,  
207 shrubs, trees and total fuel load) at the plot level across the complex gradient of  
208 Cerrado formations (i.e., grassland, savanna and forest) in Brazil from field and  
209 simulated GEDI data; and ii) characterize large-scale, multi-layer fuel loads across  
210 the entire Cerrado (i.e. 1.9 million km<sup>2</sup>) by applying the calibrated RF models to on-  
211 orbit GEDI data collected over its whole extent, and then aggregating the footprint  
212 level fuel load estimates to 1-km-resolution grid across the biome.

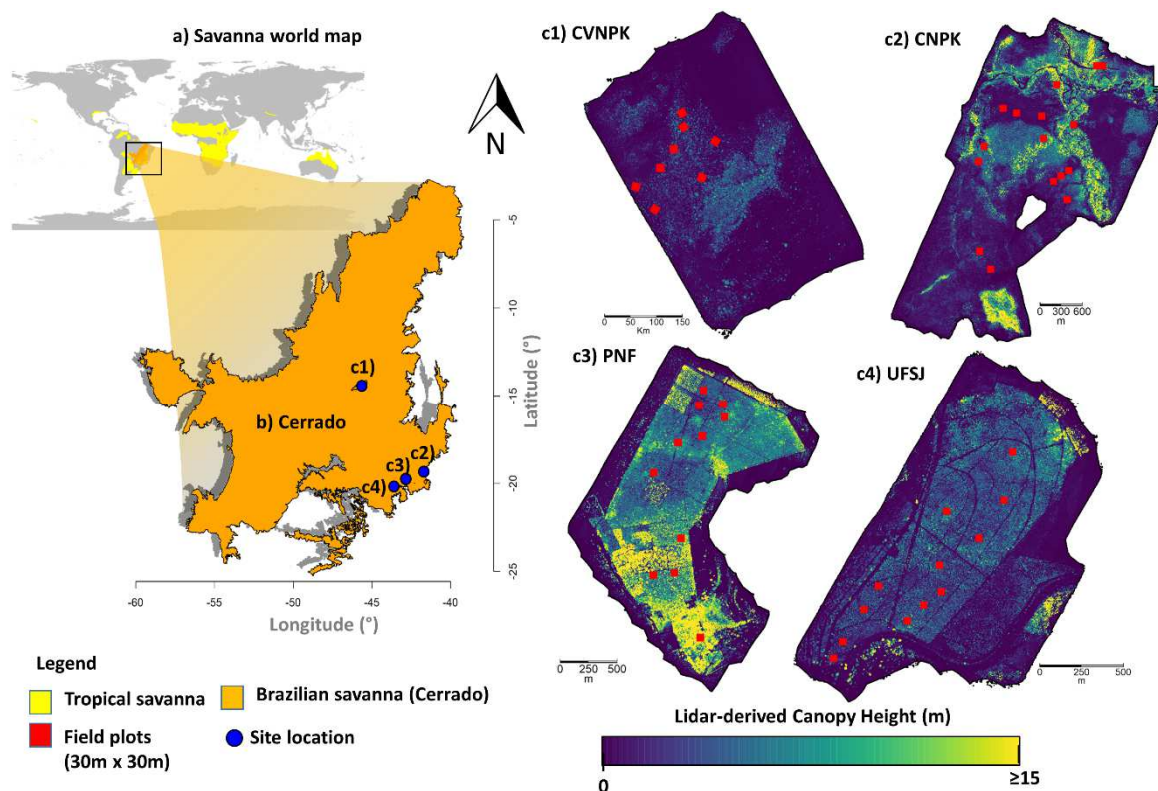
## 213 **2. Material and Methods**

### 214 **2.1. Study area**

215 The Brazilian Cerrado is the most biodiverse savanna in the world and  
216 considered as a top global hotspot for conservation priorities (Myers et al. 2000). It  
217 has been rapidly converted to crop and pasturelands and less than half of its original  
218 vegetation cover remains (Strassburg et al. 2017). This native vegetation, however,  
219 has been severely impacted by human-mediated shifts in fire regimes and  
220 widespread invasion of fire-prone African fodder grasses (Durigan and Ratter, 2016).  
221 Our study sites are located in the Serra do Cipó National Park (SCNPK), Chapada  
222 dos Veadeiros National Park (CVNPK), Paraopebas National Forest (PNF) and  
223 University of São João Del-Reis Forest (UFSJ) (Fig. 1). Site locations were chosen to  
224 span a range of vegetation structures within the Cerrado biome, covering the three



225 major formations (i.e., grassland, savanna, and forest). In Cerrado, grasslands are  
 226 characterized by the presence of grass species alone (vegetation type locally known  
 227 as “Campo limpo”), with scattered shrubs (“Campo sujo” and “Campo rupestre”), or  
 228 dominated by grasses and shrubs with scattered trees (“Cerrado ralo”). The savanna  
 229 formation is mostly dominated by contorted short trees with scattered shrubs and  
 230 grasses (e.g., “Cerrado sensu stricto”). Forests are tree-dominated formations (e.g.,  
 231 “Cerradão”, in addition to the extra-Cerrado forest formations as Riparian and  
 232 Gallery forests). For further study site characteristics regarding their location,  
 233 seasonal/climate traits, soil characteristics and topography, please refer to section 2.1  
 234 in [Costa et al. \(2021\)](#).



235

236 **Fig. 1.** Spatial location of the Brazilian savanna (Cerrado) (a, b) and study sites where  
 237 UAV-lidar and field data were collected, namely, Chapada dos Veadeiros National

238 Park (CVNPK, c1), Serra do Cipó National Park (SCNPK, c2) Paraopeba National  
239 Forest (PNF, c3) and University of São João Del-Rei's Forest (UFSJ, c4). Fig.c1-c4  
240 show the UAV-lidar coverage and canopy height model derived from the 3D point  
241 cloud.

## 242 **2.2 Fuel load measurements**

243 We established sample plots in different Cerrado vegetation formations (i.e.,  
244 grassland, savanna, and forest) between June and July 2019. First, 50 square plots of  
245 30 x 30 m (900 m<sup>2</sup>) were set across the study sites (Fig. 2a). Each plot corner was  
246 geolocated using a Differential Global Navigation Satellite System (Fig. 2c).  
247 Subsequently, four 1 x 1 m (1 m<sup>2</sup>) and two 1 x 5 m (5 m<sup>2</sup>) subplots were set within  
248 each plot to measure surface and shrubs/small trees fuel components, respectively  
249 (Fig. 2b, 2d). In the field, all duff, litter and downed woody debris (surface fuels;  
250  $SU_{fuels}$ ) were separated from non-woody grasses, herbs and forbs (herbaceous fuels;  
251  $HB_{fuels}$ ). They were immediately weighed with a 10 g precision scale. Three 500 g  
252 samples were taken to be weighed on a laboratory scale (precision of 1 mg) and oven  
253 dried at 65°C until a constant weight was reached. The fresh and dry weight of the  
254 samples were used to calculate fuel moisture content (FMC, Eq. 1). The total dry  
255 biomass of  $SU_{fuels}$  and  $HB_{fuels}$  were then calculated for the plots using Eq. 2 and 3. In  
256 addition,  $SU_{fuels}$  and  $HB_{fuels}$  were summed up to create a single component of the  
257 lowest stratum  $SH_{fuels}$  (Eq. 4).

$$FMC(\%) = (FW - DW)/DW, \quad (\text{eq.1})$$

258 where:  $FW$  is the sample's fresh weight (g) measured in the field and  $DW$  is its oven-  
 259 dried weight (g).

$$SU_{fuels} = \sum_{i=1}^n ((duff_i(kg) + litter_i(kg) + downed\ wood_i(kg)) \times (1 - FMC)) \times HEF_{SU}, \quad (eq.2)$$

260 where:  $SU_{fuels}$  is the total dry biomass ( $Mg\ ha^{-1}$ ) of duff, litter and downed wood  
 261 collected in sub-plot i.  $HEF_{SU}$  is the hectare expansion factor of 2.5 used to convert  
 262 from kg to  $Mg\ ha^{-1}$ .

$$HB_{fuels} = \sum_{i=1}^n ((non - woody\ grasses_i(kg) + forbs_i(kg)) \times (1 - FMC)) \times HEF_{SU}, \quad (eq.3)$$

263 where:  $HB_{fuels}$  is the total dry biomass ( $Mg\ ha^{-1}$ ) in plot i of non-woody grasses and  
 264 forbs collected in subplot j.

$$SH_{fuels} = SU_{fuels} + HB_{fuels}, \quad (eq.4)$$

265 where:  $SH_{fuels}$  is the total dry biomass ( $Mg\ ha^{-1}$ ) of the lowest vegetation stratum.

266 Similarly, all the shrubs and trees with diameter at breast height ( $dbh$ , 1.3 m) < 10  
 267 cm were harvested and immediately weighed with a 10 g precision scale. Three 500 g  
 268 samples of stems, branches and leaves were taken to be weighed in a laboratory scale  
 269 (precision 1 mg) and oven dried at 65°C until constant weight was reached. The total  
 270 dry biomass of this component was then calculated using Eq. 5.

$$SS_{fuels} = \sum_{i=1}^n ((shrubs_i(kg) + small\ trees_i(kg)) \times (1 - FMC)) \times HEF_{SS} \quad (eq.5)$$

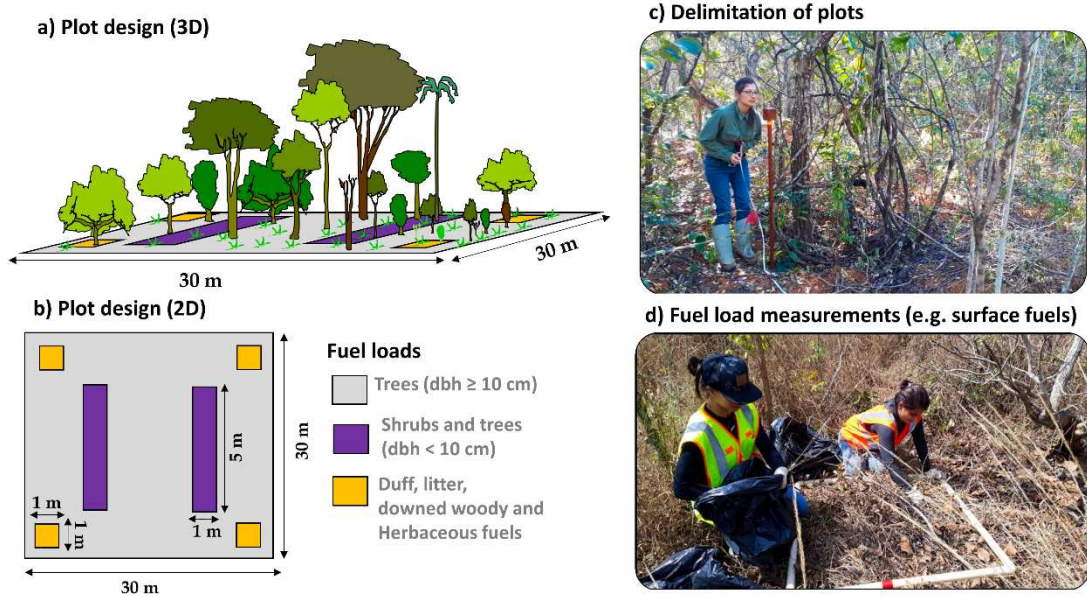
271 where:  $SS_{fuels}$  is the total dry biomass ( $Mg\ ha^{-1}$ ) of shrubs and small trees ( $dbh < 10$   
272 cm).  $HEF_{ss} = 2.5$ .

273 Finally, all the trees in the plots with  $dbh \geq 10$  cm were measured for total height  
274 ( $ht$ ) and  $dbh$  using a digital clinometer and diameter tape, respectively. We used those  
275 measurements to estimate the dry aboveground biomass of trees ( $WD_{fuels}$ ) using Eq.  
276 6 (Chave et al., 2014).

$$WD_{fuels} = \sum_{j=1}^n 0.0673 \times (\rho \times dbh_j^2 \times ht_j)^{0.976} \times HEF_{wd}, \quad (\text{eq.6})$$

277 where:  $WD_{fuels}$  is the total dry aboveground biomass of trees ( $Mg\ ha^{-1}$ );  $dbh_j$  and  $ht_j$   
278 are the  $dbh$  (cm) and  $ht$  (m) per tree  $j$ ;  $\rho$  is the wood density ( $g\ cm^{-3}$ ) derived from  
279 Zanne et al. (2009).  $HEF_{wd} = 0.011$ . The total fuel load ( $TF_{fuels}$ ) was calculated by  
280 summing all the components (Eq. 7). Table 1 summarizes fuel load component values  
281 in the sample plots by each Cerrado formation and a description of the data  
282 collection authorization process is in the supplementary material.

$$TF_{fuels} = SU_{fuels} + HB_{fuels} + SS_{fuels} + WD_{fuels} \quad (\text{eq.7})$$



283

284 **Fig. 2.** Summary of field data survey where different plot sizes were designed for  
 285 collecting tree, shrub, and surface fuels (a, b). Subfigures c) and d) depict plot  
 286 sampling configuration and surface fuel collection, respectively.

287 **Table 1.** Summary of field measurements of surface fuels ( $SU_{fuels}$ ), herbaceous  
 288 ( $HB_{fuels}$ ), surface and herbaceous fuels ( $SH_{fuels}$ ), shrubs ( $SS_{fuels}$ ,  $dbh < 10$  cm), woody  
 289 fuels ( $WD_{fuels}$ ,  $dbh \geq 10$  cm) and total fuel load ( $TF_{fuels}$ ) over the different Cerrado  
 290 formations (i.e., grassland, savanna and forests).

291

Cerrado formation	Number of plots	Fuel component	Fuel load ( $Mg\ ha^{-1}$ )			
			min	max	mean	sd
Grassland	5	$SU_{fuels}$	2.7	10.3	5.1	3.1
		$HB_{fuels}$	3.7	19.9	10.6	6.8
		$SH_{fuels}$	6.6	25.6	15.7	8.5
		$SS_{fuels}$	0.1	4.5	1.4	1.8
		$WD_{fuels}$	0.0	0.6	0.1	0.3
		$TF_{fuels}$	11.7	25.9	17.2	7.3
Savanna	30	$SU_{fuels}$	2.0	22.4	8.0	4.1
		$HB_{fuels}$	0.6	7.7	3.7	1.9
		$SH_{fuels}$	3.8	26.1	11.7	4.5
		$SS_{fuels}$	0.5	39.7	10.1	9.2
		$WD_{fuels}$	0.0	55.6	18.6	17.1
		$TF_{fuels}$	13.3	100.2	40.4	23.5
Forest	15	$SU_{fuels}$	0.8	30.1	13.9	7.3
		$HB_{fuels}$	0.4	6.7	1.3	1.6

$SH_{fuels}$	1.3	30.7	15.3	7.8
$SS_{fuels}$	0.0	36.8	11.9	13.1
$WD_{fuels}$	25.9	138.1	77.1	39.2
$TF_{fuels}$	43.7	187.9	104.2	42.4

292

### 293 2.3. UAV-lidar data acquisition and processing

294 The UAV-lidar 3-D point clouds were acquired with the GatorEye Gen 1 UAV  
295 system (Broadbent et al., 2021) in July 2019. The GatorEye platform was a DJI M600  
296 Pro hexacopter that integrated a Velodyne VLP-32c dual-return laser scanner lidar  
297 with an Inertial Measurement Unit (Fig. 3), and it was coupled with a dual-return  
298 lidar sensor with 32 separate lasers, each having a 360° vertical field of view (FOV).  
299 The sensor emitted around 600,000 pulses per second with a theoretical return  
300 number of 1.2 million returns per second and in parallel, a Global Navigation  
301 Satellite System (GNSS) receiver collected static geolocation data to calculate a post-  
302 processing kinematic (PPK) flight trajectory. Herein, UAV-lidar 3D point cloud data  
303 processing included implementing the GatorEye Multi-scalar Post-Processing  
304 Workflow (as detailed in Broadbent et al., 2021), aligning the flight lines, and  
305 clipping the point clouds within the field plots for GEDI data simulation (Section  
306 2.4).



307

308 **Fig. 3.** GatorEye UAV-lidar (Gen 1) system. a) DJI M600 Pro hexacopter, with  
309 Phoenix Scout Ultra, hyperspectral, and visual sensors; b) three GNSS antennas for  
310 navigation, and one for sensor trajectory (positioned in the middle); c) Velodyne  
311 Ultra Puck lidar system.

## 312 **2.4. GEDI data**

### 313 **2.4.1. GEDI full-waveform simulation**

314 We simulated GEDI data from the UAV-lidar 3D point cloud for calibrating fuel  
315 load models to avoid the geolocation errors of GEDI (~10-20 m) and due to the fact  
316 that GEDI orbits are likely not to overlay our field plots. The GEDI pre-launch plan  
317 included the development of a GEDI simulator that is able to reproduce the on-orbit  
318 GEDI data characteristics for the calibration of aboveground biomass models  
319 (Hancock et al., 2019). The simulation includes transforming discrete-return lidar  
320 point clouds into full-waveform signals (Blair and Hofton 1999) in GEDI-sized  
321 footprints and with the expected GEDI instrument noise added. The waveform  
322 signal-to-noise ratio (SNR) on the on-orbit GEDI data depends on characteristics such  
323 as laser type (power or coverage), acquisition time (day or night), canopy cover and  
324 atmospheric conditions (Hancock et al., 2019, Dubayah et al., 2020a, Ducanson et al.,  
325 2020). The simulator ensures consistency across point cloud flight characteristics

326 especially for high-density lidar point clouds, as used as input in this study, that  
327 allow consistently transferring models to the on-orbit GEDI data. Complete  
328 description and validation of the GEDI simulator are described in detail in [Hancock](#)  
329 [et al., 2019](#). GEDI-like waveforms were simulated from the high-density UAV-lidar  
330 point clouds clipped to the study sample plots using the *gediWFSimulator* tool in the  
331 rGEDI package ([Silva et al., 2020](#)) in R ([R Core Team 2020](#)). Realistic noise was added  
332 considering a beam sensitivity of 0.98 (i.e., the canopy cover at which ground is  
333 detected 90% of the time with 5% probability of a false positive [Hancock et al. \(2019\)](#))  
334 by using a link margin of 4.956 at 95% of canopy cover that relates to noise of the  
335 power beam collecting data at night ([Boucher et al., 2020](#)). For ground detection and  
336 metrics calculation, the waveforms were denoised and smoothed by setting the noise  
337 threshold as the mean plus 3 standard deviations and smoothing width (applied after  
338 denoising) equal to 0.5 m ([Qi et al., 2019](#), [Silva et al., 2021](#)).

#### 339 **2.4.2. GEDI-derived vegetation structure metrics**

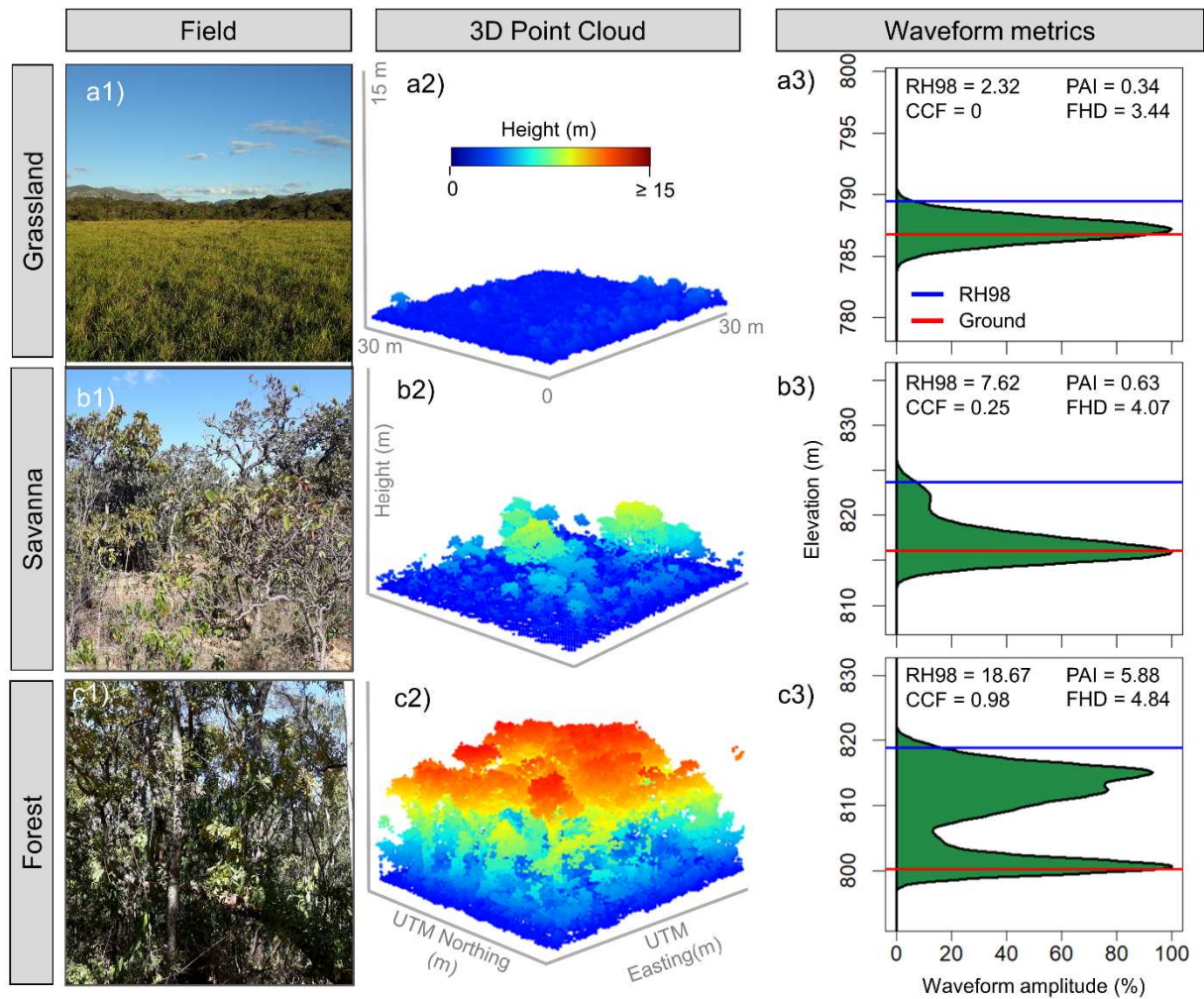
340 We calculated the following metrics from the simulated GEDI full-waveforms  
341 ([Table 2](#)): RH (relative height) at the 98th height percentile (RH98, in m), canopy  
342 cover fraction (CCF, in %), plant area index (PAI, in  $\text{m}^2 \text{m}^{-2}$ ), and Foliage Height  
343 Diversity (FHD, unitless). These metrics were selected to match to the GEDI Level 2A  
344 and 2B products and facilitate model interpretability. RH98 represents the height  
345 below which 98% of the returned laser energy is registered. It was selected to  
346 represent the top of the canopy, avoiding the noise of using the last return elevation



347 value (Silva et al. 2018). The CCF is related to the percent of the ground covered by  
 348 the vertical projection of canopy material calculated from the Gaussian fitted ground  
 349 signal. PAI is the projected area of plant elements per unit ground surface, which  
 350 relates to the canopy cover and plant occupation of the vertical space. The FHD is an  
 351 index for expressing canopy structure complexity and vertical distribution  
 352 (MacArthur and Horn 1969). It is calculated by summing the product between the  
 353 proportion of vertical PAI profiles and its logarithm in a selected horizontal layer  
 354 (Tang and Armston, 2019). The theoretical basis and full description of cover and  
 355 vertical profile GEDI metrics are detailed in the algorithm theoretical basis document  
 356 (Tang and Armston, 2019). The metrics were calculated using the *gediWFMetrics*  
 357 function in rGEDI (Silva et al., 2020) (Fig. 4).

358 **Table 2.** GEDI waveform metrics used as predictors to estimate fuel load components

<b>Acronym</b>	<b>Description</b>
RH98	Relative height at the 98th height percentile (m)
PAI	Plant Area Index (m <sup>2</sup> m <sup>-2</sup> )
CCF	Canopy cover fraction (%)
FHD	Foliage Height Diversity (unitless)



359

360 **Fig. 4.** Cerrado formations (a1, b1, and c1) and respective 3D point clouds from a  
 361 UAV lidar survey (a2, b2, and c2) and metrics from the simulated waveforms (a3, b3,  
 362 and c3).

### 363 2.5 Fuel load modeling development

364 Principal Component Analysis (PCA) was applied using the R package  
 365 FactoMineR (Lê et al., 2008) for characterizing fuel load and GEDI metrics across  
 366 field plots and vegetation formations. An explorative analysis of the derived PC  
 367 scores was conducted in the first two components to analyze the relationships  
 368 between field and GEDI variables.

369 Fuel loads were modeled separately, yielding five models with the GEDI metrics

370 as predictors and  $SU_{fuels}$ ,  $HB_{fuels}$ ,  $SH_{fuels}$ ,  $SS_{fuels}$ ,  $WD_{fuels}$  and  $TF_{fuels}$  as response  
371 variables. We used the random forest (RF) algorithm implemented through the Caret  
372 R package (Kuhn 2020) as our modeling approach. RF builds regression tree  
373 ensembles from bootstrapping the data, and the final prediction is the average  
374 ensemble outcome (Breiman et al., 1984, Breiman 1996). This method was selected for  
375 being flexible to the different data distributions present in our dataset due to the  
376 various vegetation structures in the Cerrado formations (Fig. S1). Each RF was built  
377 with 500 trees tuning the number of predictors at each split ( $m_{try}$ ). We tested  $m_{try}$   
378 ranging from two to four ( $2 \leq m_{try} \leq 4$ ), selecting the best tuned model in a 5-fold  
379 cross-validation assessment using the coefficient of determination ( $R^2$ ), absolute (Mg  
380  $ha^{-1}$ ) and relative (%) root square mean error (RMSE) and mean difference (MD) (Eq.  
381 8 to 12).

$$R^2 = 1 - \frac{\sum_{i=1}^n (Y_i - \hat{Y}_i)^2}{\sum_{i=1}^n (Y_i - \bar{Y})^2}, \quad (\text{eq.8})$$

$$RMSE (Mg / ha) = \sqrt{\frac{\sum_{i=1}^n (\hat{Y}_i - Y_i)^2}{n}}, \quad (\text{eq.9})$$

$$RMSE (\%) = \frac{RMSE}{\bar{Y}} \times 100, \quad (\text{eq.10})$$

$$MD (Mg / ha) = \frac{\sum_{i=1}^n (\hat{Y}_i - Y_i)}{n}, \quad (\text{eq.11})$$

$$MD (\%) = \frac{MD}{\bar{Y}} \times 100, \quad (\text{eq.12})$$

382 where:  $\hat{Y}_i$  is the estimated fuel load (Mg  $ha^{-1}$ ),  $Y_i$  is the observed fuel load (Mg  $ha^{-1}$ );  $n$   
383 is number of samples. For each fuel layer, the tuned model was run 500 times to  
384 account for the algorithm randomness.

## 385 2.6 Fuel loads characterization in Cerrado

386 The GEDI Level 2A and 2B version 2 data products (Dubayah et al., 2021b, ,  
387 Dubayah et al., 2021c) collected between April 18, 2019 and October 29,, 2020 were  
388 downloaded over the entire Cerrado vegetated area. The GEDI orbits intersecting  
389 Cerrado limits were found and downloaded using the *gedifinder* and *gediDownload*  
390 functions in rGEDI package (Silva et al., 2020). The footprints were masked to the  
391 Cerrado vegetated area based on the land cover classification from Mapbiomas for  
392 the same year of the data collection (Souza et al. 2020). The GEDI footprint-level  
393 metrics (Table 2) were extracted using the *getLevel2AM* and *getLevel2B* functions and  
394 filtered using the quality flag (quality\_flag = 1). This flag indicates usable data by  
395 summarizing individual quality assessment parameters based on waveform shot  
396 energy, sensitivity (< 0.9 over land), amplitude, and real-time surface tracking quality  
397 (Hofton and Blair 2019, Beck et al., 2020).

398 The fuel load models developed in item 2.5 were applied to the GEDI footprints  
399 (diameter of ~25 m) collected across the Cerrado biome extent. Fuel load maps of  
400 each component were created by taking the average of the footprint-level estimates  
401 at 1-km<sup>2</sup> grid cells for mapping purposes and compatibility with planned gridded  
402 GEDI products (Dubayah et al., 2020a) and requirements for global biomass maps  
403 (Hall et al., 2011).

404 We calculated the uncertainty of fuel load predictions in each cell by accounting  
405 for the footprints' variability within the cell, uncertainty associated with the RF  
406 algorithm, and RF lack of fit. To show this we start by assuming that the fuel load

407 estimate at footprint i with model m is given:

$$RF_{im} = \theta_i + e_{im}, \quad (\text{eq.13})$$

408 where  $\theta_i$  is the overall mean prediction for footprint i and  $e_{im}$  is an error term. We  
409 assume that the expected value and variance of this error are  $E[e_{im}] = 0$  and  
410  $Var[e_{im}] = \tau_i^2$ , respectively. The parameter  $\tau_i^2$  captures the within-footprint  
411 variability associated with the randomness of the RF algorithm. We also assume that  
412 the RF mean prediction  $\theta_i$  is given by:

$$\theta_i = \mu_i + \epsilon_i \quad (\text{eq.14})$$

413

414 where  $\mu_i$  is the true biomass of footprint i and  $\epsilon_i$  is another error term. This error term  
415 accounts for the fact that mean RF prediction is not identical to the true biomass. We  
416 assume that  $E[\epsilon_i] = 0$  and  $Var[\epsilon_i] = \psi^2$ , where  $\psi^2$  quantifies the uncertainty  
417 associated with the lack of fit of the RF model. These equations imply that:

$$RF_{im} = \mu_i + \epsilon_i + e_{im}. \quad (\text{eq.15})$$

418

419 The fuel load prediction at footprint i is then given by the average of the RF  
420 models applied to footprint i:

$$\overline{RF}_i = \frac{\sum_m RF_{im}}{M} = \frac{M\mu_i}{M} + \frac{M\epsilon_i}{M} + \frac{\sum_m e_{im}}{M} = \mu_i + \epsilon_i + \frac{\sum_m e_{im}}{M} \quad (\text{eq.16})$$

421

422 where  $\overline{RF}_i$  is the mean fuel load estimate at footprint i and M is the number of RF  
423 models that were fit. Assuming no correlation between lack of model fit ( $\epsilon_i$ ) and  
424 differences between RF models ( $e_{im}$ ), this implies that:

$$Var(\overline{RF}_i|\mu_i) = \psi^2 + \frac{\tau_i^2}{M} \quad (\text{eq.17})$$

425

426

Recall that we took the average of all GEDI footprint-level fuel load predictions

427

within a 1-km<sup>2</sup> cell. Assuming no spatial correlation in the mean fuel load in each

428

footprint and model lack of fit, we have that the uncertainty associated with each cell

429 is:

$$Var(\overline{RF}_k) = Var\left(\frac{\sum_i \overline{RF}_{ik}}{n_k}\right) = Var\left(\frac{\sum_i \mu_{ik}}{n_k} + \frac{\sum_i \epsilon_{ik}}{n_k} + \frac{\sum_i \frac{\sum_m e_{imk}}{M}}{n_k}\right) \quad (\text{eq.18})$$

430

431 where  $n_k$  is the number of GEDI footprints within the 1-km<sup>2</sup> cell (k).

432

If we assume that the uncertainty associated with model lack of fit ( $\psi^2$ ) does not

433 vary from footprint to footprint, then:

$$= Var\left(\frac{\sum_i \mu_{ik}}{n_k}\right) + Var\left(\frac{\sum_i \epsilon_{ik}}{n_k}\right) + Var\left(\frac{\sum_i \frac{\sum_m e_{imk}}{M}}{n_k}\right) \quad (\text{eq.19})$$

$$= Var\left(\frac{\sum_i \mu_{ik}}{n_k}\right) + \frac{n_k \psi^2}{n_k^2} + \frac{1}{n_k^2} \left( \sum_i \frac{M \tau_{ik}^2}{M^2} \right) \quad (\text{eq.20})$$

$$= Var\left(\frac{\sum_i \mu_{ik}}{n_k}\right) + \frac{\psi^2}{n_k} + \frac{\sum_i \tau_{ik}^2}{n_k^2 M} \quad (\text{eq.21})$$

434

435

Finally, if we assume that  $E[\mu_{ik}] = m_k$  and  $Var[\mu_{ik}] = \delta_k^2$ , then the overall

436 uncertainty at each cell (k) is given by:

$$= \frac{\delta_k^2}{n_k} + \frac{\psi^2}{n_k} + \frac{\sum_i \tau_{ik}^2}{n_k^2 M} \quad (\text{eq.22})$$

437

438

This expression shows that the variance for each cell k can be partitioned into the

439 variability of biomass within each cell k (captured by  $\delta_k^2$ ), model lack of fit (captured  
 440 by  $\psi^2$ ) and RF uncertainty (captured by  $\tau_{ik}^2$ ). Notice that, as the number of GEDI  
 441 footprints within cell k increases (i.e.,  $n_k$  increases), then overall uncertainty  
 442 decreases. Furthermore, increasing the number of RF models (i.e., M) only decreases  
 443 the last uncertainty piece.

444 For each cell, we estimated  $\delta_k^2$  and  $\hat{\tau}_{ik}^2$  with the following equations:

$$\delta_k^2 = \frac{\sum_i (\overline{RF}_{ik} - \overline{RF}_k)^2}{n_k - 1} \quad (\text{eq.23})$$

$$\hat{\tau}_{ik}^2 = \frac{\sum_m (RF_{ikm} - \overline{RF}_{ik})^2}{M - 1} \quad (\text{eq.24})$$

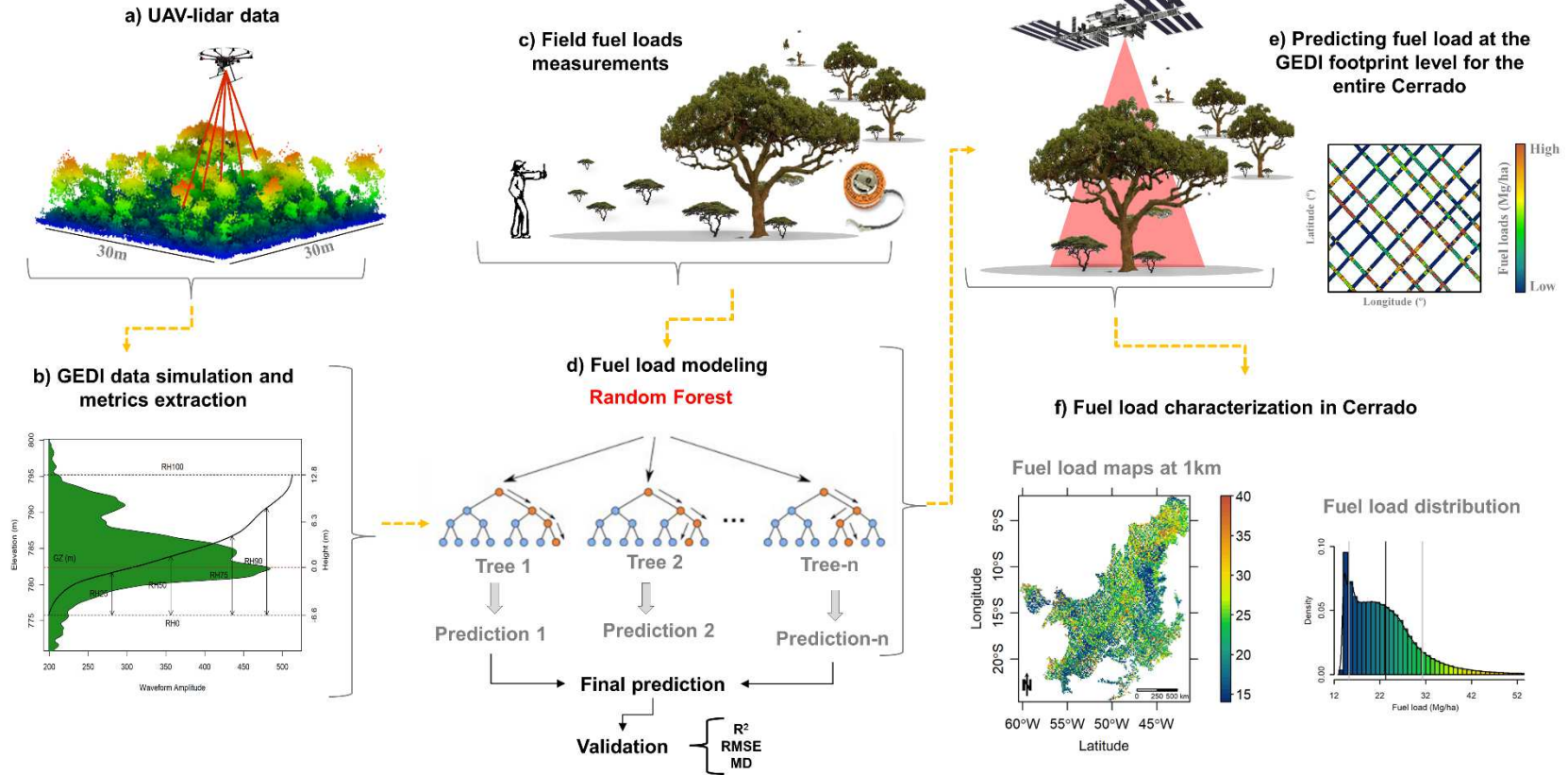
445

446 where  $\overline{RF}_{ik}$  is the mean fuel load prediction of footprint i in cell k,  $\overline{RF}_k$  is the mean  
 447 fuel load prediction in cell k,  $\overline{RF}_{ikm}$  is the fuel load prediction of footprint i in cell k  
 448 using RF model m. The only variance parameter that is estimated separately using  
 449 the field data is the lack of fit parameter (i.e.,  $\psi^2$ ). The estimation of this parameter is  
 450 described in the supplementary material. The uncertainty is presented in absolute  
 451 values by taking the square-root of the summed variance parameters. A workflow  
 452 summarizing the full methodology applied in this study is provided in [Fig. 5](#).

### UAV-lidar and GEDI simulations

### Fuel load modeling

### Large scale fuel load characterization



453

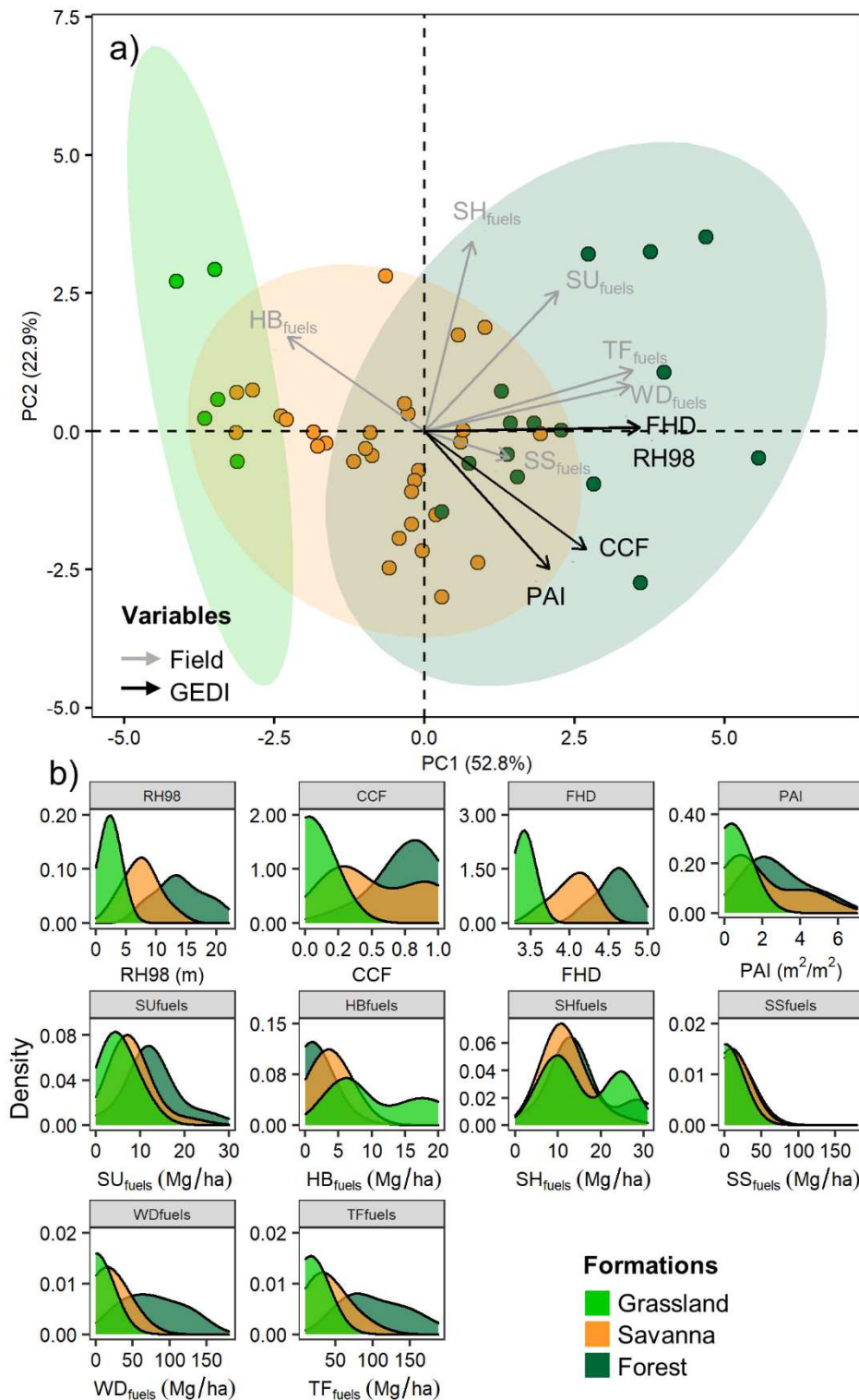
454 **Fig. 5.** Workflow to estimate fuel load components in Cerrado using GEDI data. High density UAV-lidar point clouds were  
 455 collected (a) from which GEDI-like waveforms were simulated (b). The models were created using fuel load measurements from  
 456 the field (c) as response variables in a random forest (RF) model and GEDI waveform metrics as predictors (d). The RF models were  
 457 applied to the 25-m GEDI footprints in Cerrado (e) and averaged into 1-km grid cells (f).



## 458 3. Results

### 459 3.1. Exploratory analysis of GEDI metrics and fuel components in the Cerrado 460 formations

461 The PCA biplot shows distinct scores for the Cerrado formations and these first  
462 two PCs were responsible for 75.7% of the variables' cumulative variance (Fig. 6a).  
463 The RH98 and FHD showed high correlation with each other ( $r = 0.94$ ,  $p\text{-value} = 2.2E\text{-}$   
464  $16$ ) and were the two metrics mainly explaining the variability in PC1 being, overall,  
465 positively correlated to samples in the forest formation and negatively correlated  
466 with grassland observations. The fuel components that were most correlated with  
467 RH98 and FHD were  $WD_{fuels}$  ( $r > 0.85$ ,  $p\text{-value} < 2.2E\text{-}15$ ) and  $TF_{fuels}$  ( $r > 0.82$ ,  $p\text{-value}$   
468  $< 1.3E\text{-}13$ ).  $SU_{fuels}$  had a weaker relationship ( $r < 0.51$ ,  $p\text{-value} < 0.0008$ ) with the  
469 GEDI variables, though higher values were found in forests (Fig. 6b). Similarly,  
470  $SH_{fuels}$  had lower correlations ( $r < |0.30|$ ,  $p\text{-value} < 0.03$ ) with the GEDI variables  
471 than its sub-components  $SU_{fuels}$  ( $r < 0.52$ ,  $p\text{-value} < 0.0008$ ) and  $HB_{fuels}$  ( $r < |0.59|$ ,  $p\text{-}$   
472  $value < 0.002$ ). The grassland observations showed opposite scores on PC1 compared  
473 to the forest observations and were mostly represented by the variation in  $HB_{fuels}$ ;  
474 this is consistent with the dominance of herbaceous species in these formations (Fig.  
475 S2) indicated by the negative correlation of  $HB_{fuels}$  with the metrics CCF and PAI.  
476 The savanna formation lies near the center, overlapping with the other two  
477 formations. This is also depicted in the variables' distributions (Fig. 6b), where most  
478 of the GEDI waveform metrics showed increasing values from grasslands to forests.



479

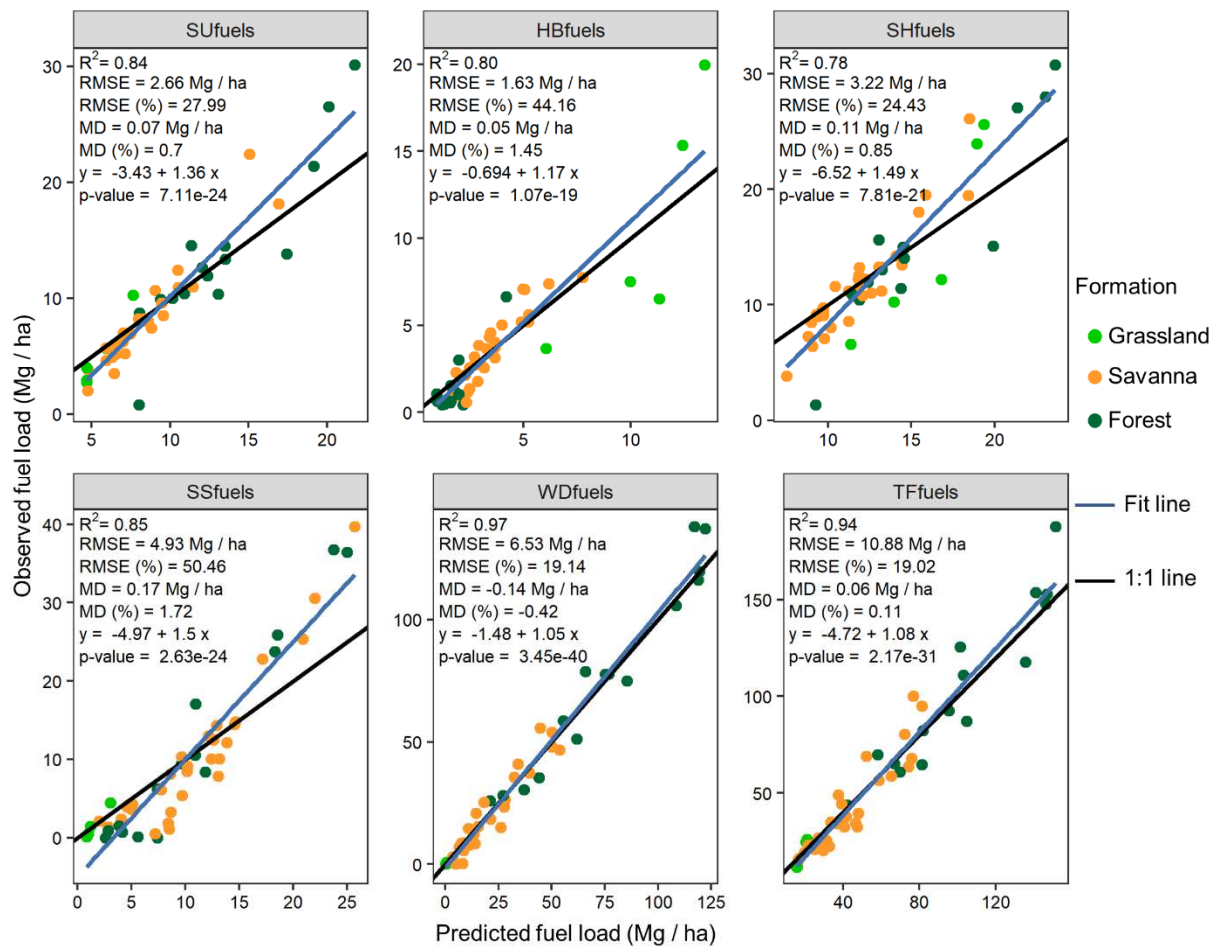
480 **Fig. 6.** Biplot of the first two axes of a principal component analysis of simulated  
 481 GEDI waveforms metrics and field fuel load measurements (a) and their respective  
 482 density plots (b). RH98 = Relative height at the 98 th height percentile; CCF = canopy  
 483 cover fraction; FHD = Foliage Height Diversity; PAI = Plant Area Index;  $SU_{fuels}$  =  
 484 surface fuels (duff, litter, downed wood);  $HB_{fuels}$  = Herbaceous fuels;  $SH_{fuels}$  =  
 485  $SU_{fuels} + HB_{fuels}$ ;  $SS_{fuels}$  = shrubs and small trees (diameter at 1.3 m above ground

486 (dbh) < 10 cm);  $WD_{fuels}$  = woody fuels (trees with dbh > 10 cm);  $TF_{fuels} = SU_{fuels} +$   
487  $HB_{fuels} + SS_{fuels} + WD_{fuels}$ .

488

### 489 3.2 Fuel load models

490 Overall, all models presented relatively good performance during training with  $R^2 > 0.78$ ,  
491  $RMSE < 10.83 \text{ Mg ha}^{-1}$ ,  $MD < 0.17 \text{ Mg ha}^{-1}$  (Fig. 7). The  $WD_{fuels}$  and  $TF_{fuels}$  components  
492 were more accurately estimated with models, yielding  $R^2$  values of 0.88 and 0.71,  
493 respectively, and  $RMSE$  of both  $\sim 40 \text{ Mg ha}^{-1}$  in the validation (Table 3). On the other hand,  
494 the models estimating components at the lower stratum ( $SU_{fuels}$ ,  $HB_{fuels}$ ,  $SH_{fuels}$ ) exhibited  
495 moderate to low performance during validation ( $R^2 < 0.46$ ). The estimates were less accurate  
496 when estimating the surface and herbaceous components in a single model (i.e.,  $SH_{fuels}$ ;  $R^2 =$   
497  $0.17$ ,  $RMSE = 6.22 \text{ Mg ha}^{-1}$ ,  $MD = 0.31 \text{ Mg ha}^{-1}$ ) than in separate models; i.e., for  $HB_{fuels}$   
498 ( $R^2 = 0.46$ ,  $RMSE = 2.81 \text{ Mg ha}^{-1}$ ,  $MD = 0.12 \text{ Mg ha}^{-1}$ ) and for  $SU_{fuels}$  ( $R^2 = 0.31$ ,  $RMSE =$   
499  $5.22 \text{ Mg ha}^{-1}$ ,  $MD = 0.13 \text{ Mg ha}^{-1}$ ) individually. Differences in the training-validation  
500 performance were higher for  $SH_{fuels}$  and  $SS_{fuels}$ .



501

502 **Fig. 7.** Training results for estimating surface fuels ( $SU_{fuels}$ ), herbaceous fuel ( $HB_{fuels}$ ),  
 503 surface and herbaceous fuels ( $SH_{fuels}$ ), shrub ( $SS_{fuels}$ ), tree ( $WD_{fuels}$ ) and total fuel  
 504 load ( $TF_{fuels}$ ) using Random Forest and GEDI waveform metrics as predictors. R<sup>2</sup> =  
 505 coefficient of determination; RMSE = root mean square error; and MD = mean  
 506 difference.

507

508 **Table 3.** Cross-validation performance assessment in 500 iterations of models used to  
 509 estimate surface fuels ( $SU_{fuels}$ ), herbaceous fuel ( $HB_{fuels}$ ), surface and herbaceous  
 510 fuels ( $SH_{fuels}$ ), shrub ( $SS_{fuels}$ ), tree ( $WD_{fuels}$ ) and total fuel load ( $TF_{fuels}$ ). Values  
 511 represent mean  $\pm$  standard deviation.

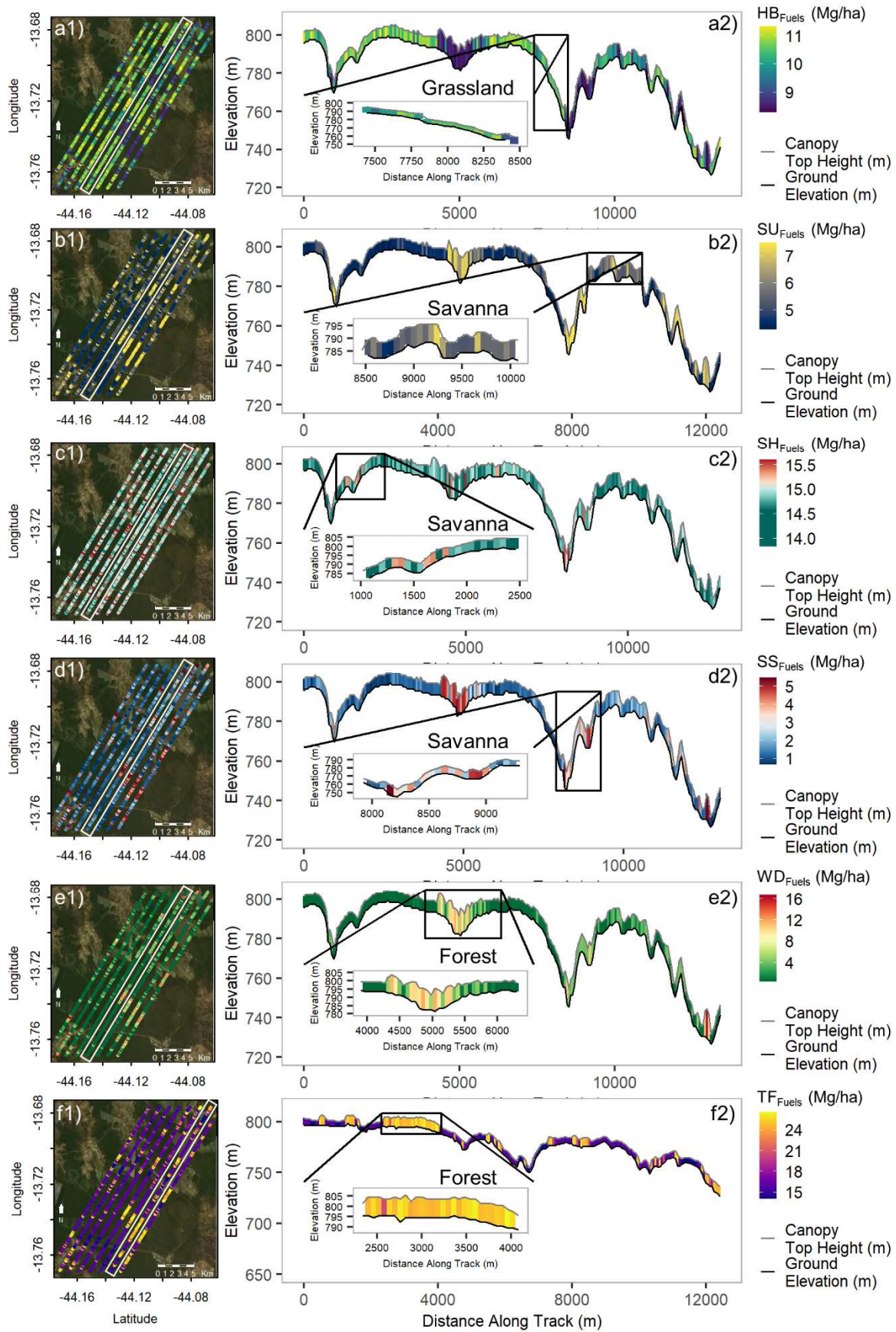
Fuel	R <sup>2</sup>	RMSE		MD	
		(Mg ha <sup>-1</sup> )	%	(Mg ha <sup>-1</sup> )	%
$SU_{fuels}$	0.31 $\pm$ 0.07	5.22 $\pm$ 0.21	55.51 $\pm$ 2.79	0.13 $\pm$ 0.18	4.61 $\pm$ 2.92
$HB_{fuels}$	0.46 $\pm$ 0.068	2.81 $\pm$ 0.2	78.6 $\pm$ 6.38	0.12 $\pm$ 0.14	10.01 $\pm$ 5.46
$SH_{fuels}$	0.17 $\pm$ 0.064	6.22 $\pm$ 0.34	47.49 $\pm$ 2.89	0.31 $\pm$ 0.28	4.04 $\pm$ 2.57
$SS_{fuels}$	0.15 $\pm$ 0.062	10.55 $\pm$ 0.5	113.32 $\pm$ 11.09	0.35 $\pm$ 0.35	16.01 $\pm$ 10.87
$WD_{fuels}$	0.88 $\pm$ 0.029	13.07 $\pm$ 0.67	40.6 $\pm$ 3.64	-0.32 $\pm$ 0.67	1.51 $\pm$ 2.83
$TF_{fuels}$	0.71 $\pm$ 0.052	23.01 $\pm$ 1.13	40.78 $\pm$ 2.4	0.22 $\pm$ 0.94	2.09 $\pm$ 2.12

512  $R^2$  = coefficient of determination; RMSE = root mean square error; and MD = mean  
513 difference.

### 514 3.3 Fuel loads characterization across the Cerrado biome

515 Fuel load estimates were obtained from the application of the models to the on-  
516 orbit GEDI data. The estimates were obtained for the entire Cerrado biome in the 25  
517 m-radii GEDI footprints. In a Cerrado subset (Fig. 8), gradients of fuel load  
518 associated with topography were observed in the different formations. For instance,  
519 there was a pattern of higher  $WD_{fuels}$  and  $TF_{fuels}$  estimates in forests (Fig. 8 e2 and  
520 f2) than in the other formations (Fig. 8 a2 - d2). On the other hand,  $HB_{fuels}$  estimates  
521 were significantly higher in grasslands (Fig. 8 a2), mainly when compared to forest  
522 formations (Fig. 8 e2 and f2). The  $SU_{fuels}$  estimates were also higher in forest  
523 formations (Fig. 8 e2 and f2) than in grasslands (Fig. 8 a2).

524



525

526 **Fig. 8.** Depiction of the GEDI footprint level estimates of fuel components showing  
 527 all the GEDI ground-tracks (a1, b1, c1, d1, e1, f1) and a single-track profile over

528 grassland, savanna, and forest formations (a2, b2, c2, d2, e2, f2). Estimates were done  
529 for surface fuels ( $SU_{fuels}$ ), herbaceous fuels ( $HB_{fuels}$ ), surface and herbaceous fuels  
530 ( $SH_{fuels}$ ), shrubs and small trees ( $SS_{fuels}$ ), woody fuels ( $WD_{fuels}$ ) and total fuel load  
531 ( $TF_{fuels}$ ).

532

533 The spatial variation of fuel components estimates in Cerrado is shown in Fig. 9.

534 These maps allowed us to identify regions in Cerrado with higher estimated  $HB_{fuels}$

535 and lower  $WD_{fuels}$  in some regions (e.g.,  $\sim 45^\circ W \sim 10^\circ S$ , Fig. 9b and d) and regions

536 with accumulated fuel as in northern Cerrado (e.g.,  $\sim 45^\circ W \sim 5^\circ S$  Fig. 9e). The

537 distribution of the estimates was mostly evenly distributed except for  $SH_{fuels}$  that

538 was slightly skewed for higher values, and  $WD_{fuels}$  and  $TF_{fuels}$  that had higher

539 frequencies of lower values (Fig. 10 a-f). The mean estimated values of  $SU_{fuels}$ ,

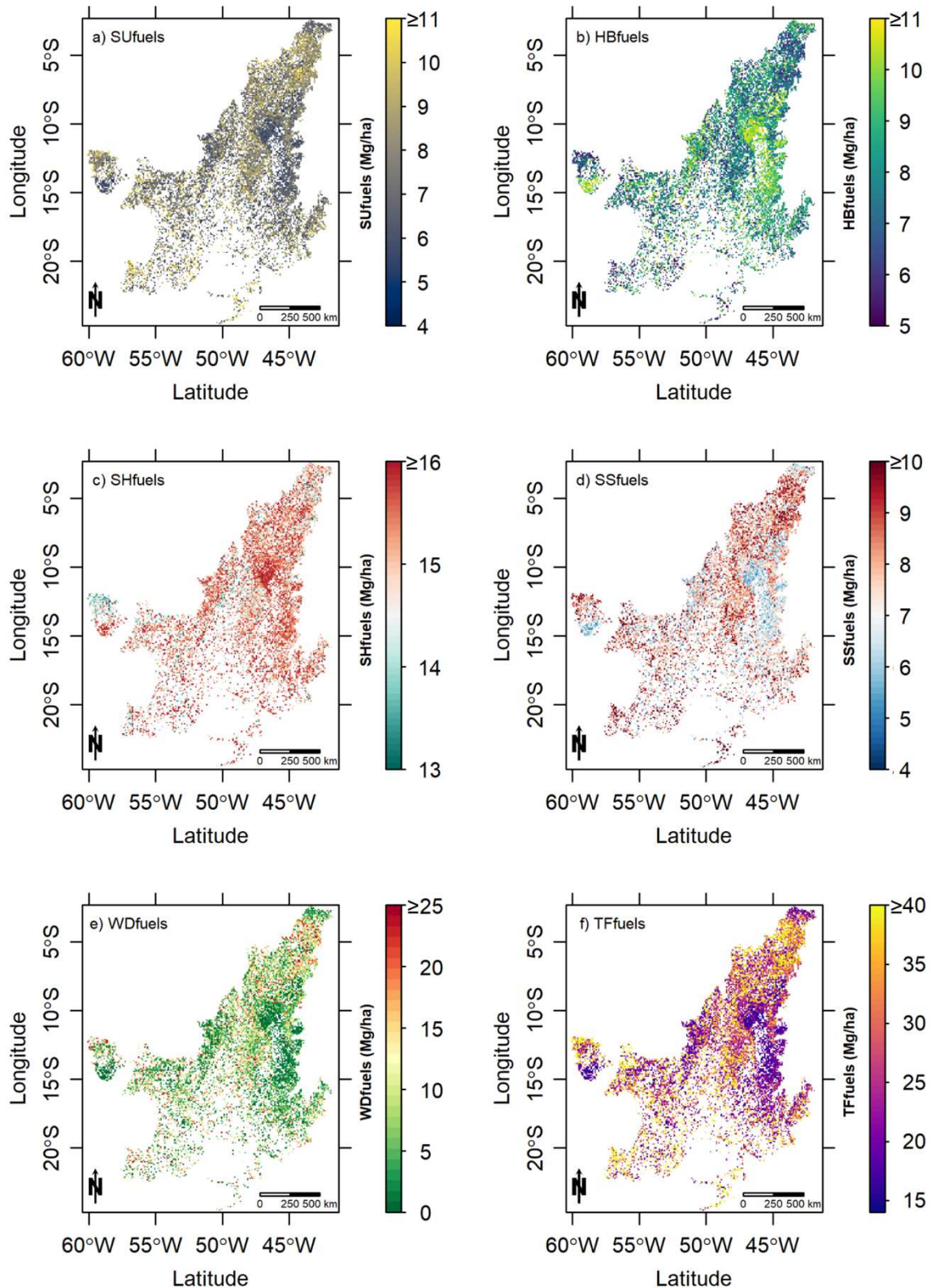
540  $HB_{fuels}$ ,  $SH_{fuels}$ ,  $SS_{fuels}$ ,  $WD_{fuels}$ , and  $TF_{fuels}$  were  $7.63 \pm 1.63$ ,  $7.87 \pm 1.78$ ,  $14.74 \pm 1.87$ ,

541  $7.58 \pm 1.64$ ,  $10.29 \pm 9.97$  and  $28.55 \pm 11.4 \text{ Mg ha}^{-1}$ , respectively. The uncertainty of the

542 predictions was similarly distributed across Cerrado (Fig. 11), with a pattern of lower

543 uncertainty in regions with more GEDI footprints (Fig. S2).

544

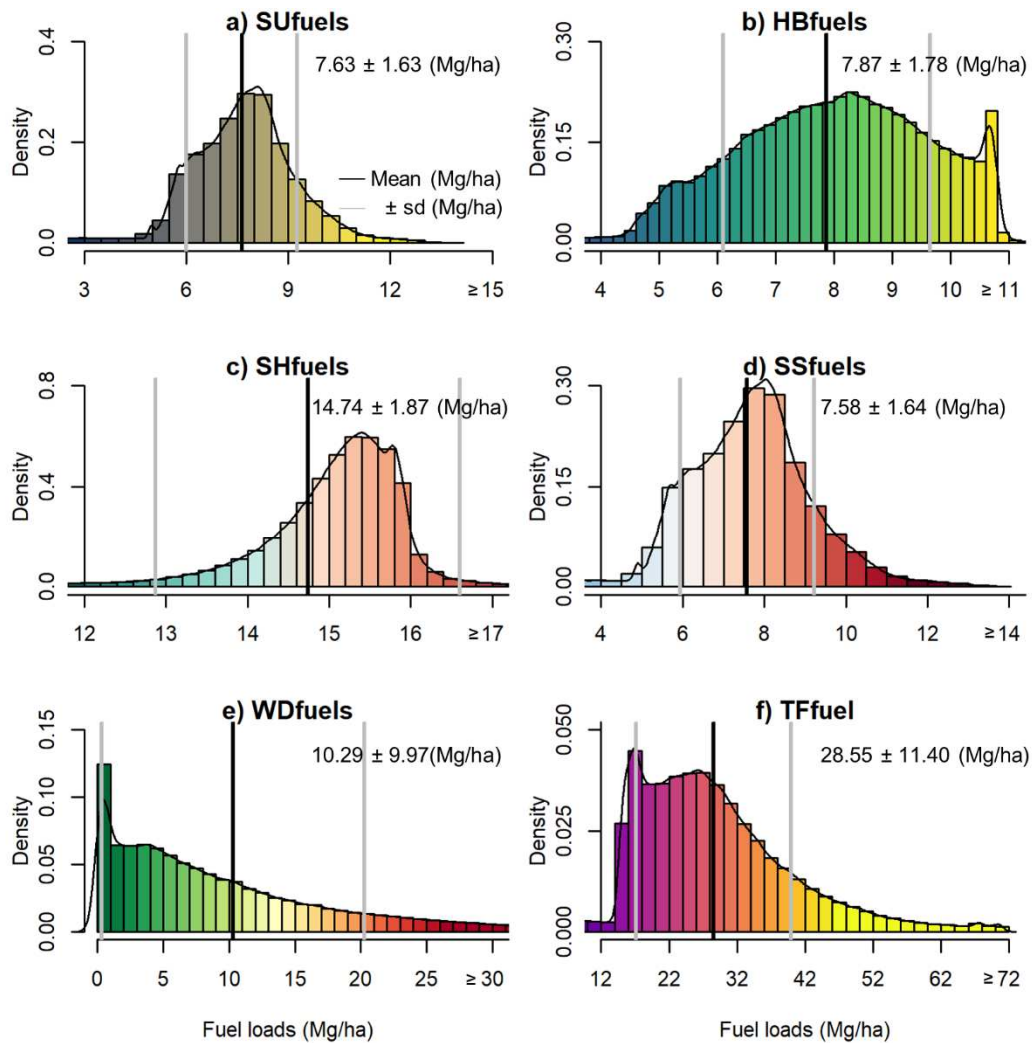


545  
 546 **Fig. 9.** GEDI-derived large scale fuel load estimates at the 1km grid cell resolution for  
 547 the entire Cerrado biome. These estimates were aggregated from the footprint-level  
 548 predictions. Surface fuels ( $SU_{fuels}$  (a)), herbaceous fuels ( $HB_{fuels}$  (b)), surface and  
 549 herbaceous fuels ( $SH_{fuels}$  (c)), shrubs and small trees fuels ( $SS_{fuels}$  (d)), woody fuels  
 550 ( $WD_{fuels}$  (e)), and the total fuel load ( $TF_{fuels}$  (f)).



551

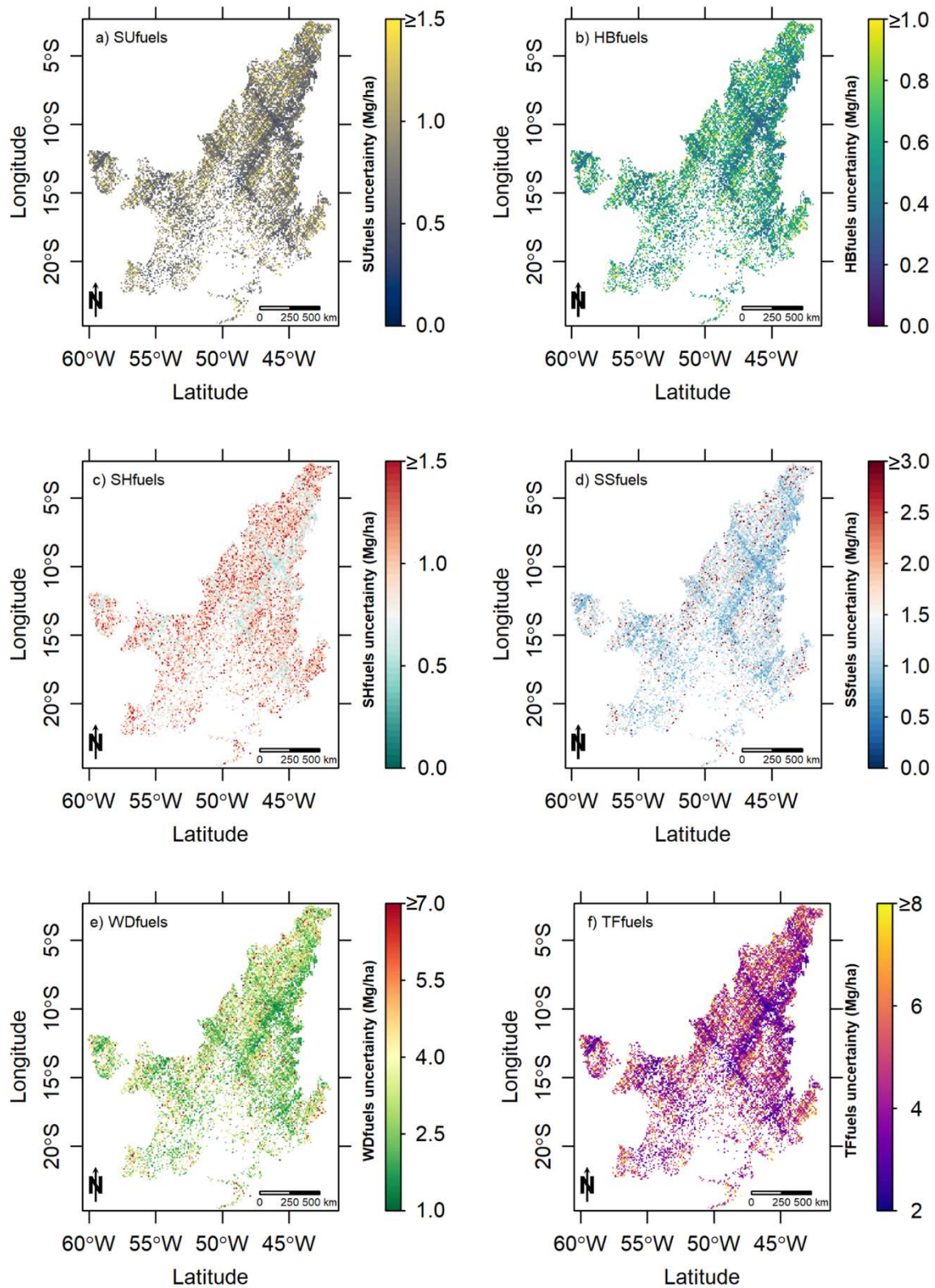
552



553

554 **Fig. 10.** Distribution of the estimates of fuel load components in Cerrado using GEDI  
555 waveform metrics and Random Forest. Separated models were trained to estimate  
556 surface fuels ( $SU_{fuels}$  (a)), herbaceous fuels ( $HB_{fuels}$  (b)), surface and herbaceous fuels  
557 ( $SH_{fuels}$  (c)), shrubs and small trees fuels ( $SS_{fuels}$  (d)), woody fuels ( $WD_{fuels}$  (e)), and  
558 the total fuel load ( $TF_{fuels}$  (f)).

559



560

561 **Fig. 11.** Uncertainty of fuel load predictions accounting for the footprints' variability

562 within the cell, uncertainty associated with the RF algorithm, and RF lack of fit.

563 Surface fuels ( $SU_{fuels}$  (a)), herbaceous fuels ( $HB_{fuels}$  (b)), surface and herbaceous fuels

564 ( $SH_{fuels}$  (c)), shrubs and small trees fuels ( $SS_{fuels}$  (d)), woody fuels ( $WD_{fuels}$  (e)), and  
565 the total fuel load ( $TF_{fuels}$  (f))

#### 566 **4. Discussion**

567 GEDI is capable of providing high resolution 3D canopy structural information of  
568 various forest ecosystems (Dubayah et al., 2020a, Schneider et al., 2020) and holds  
569 untapped potential for establishing effective forest fire management frameworks.  
570 This study demonstrated the potential of using GEDI data to estimate large-scale  
571 multi-layer fuels across the whole Brazilian Cerrado by applying both simulated and  
572 on-orbit data to model commonly used fuel load layers. The use of spaceborne lidar  
573 sensors for fuel mapping has been previously reported mainly to map canopy fuels  
574 with GLAS and ICESat-2 sensors (Ashworth et al., 2010, García et al., 2012, Peterson  
575 et al., 2013, Gwenzi et al., 2016, Narine et al., 2020). However, this is, to our  
576 knowledge, the first study demonstrating the usefulness of GEDI in estimating fuels  
577 loads at such a large geographic scale, contributing to the expansion of spaceborne  
578 lidar applications for integrated fire management activities and supporting carbon  
579 monitoring initiatives in savannas.

#### 580 **4.1. Large scale fuel load estimation using spaceborne lidar**

581 Our results demonstrated a high predictive capacity of GEDI metrics in  
582 modelling  $WD_{fuels}$  and  $TF_{fuels}$  that allows large-scale fuel load estimations. This  
583 finding is in agreement with similar studies focused on estimating biomass in  
584 different ecosystems using as predictors canopy metrics derived from spaceborne

585 lidar sensors on the satellites ICESat-1 and ICESat-2 (Xiao et al., 2019). A study  
586 carried out by Lefsky et al. (2005) in a tropical broadleaf forest in Brazil demonstrated  
587 that GLAS-derived heights were able to explain 73% of the variation in field-  
588 measured aboveground biomass. Popescu et al. (2011), who mapped aboveground  
589 biomass in a temperate forest dominated by pine and oak stands in eastern Texas,  
590 found a strong relationship ( $R^2 = 0.80$ ) between GLAS height variables and the  
591 reference biomass derived from airborne lidar data. In a more detailed study to test  
592 the capabilities of GLAS data in predicting forest aboveground biomass, Chi et al.  
593 (2015) estimated  $R^2$  values ranging from 0.64 to 0.90 over different forest zones in  
594 China. Nevertheless, it is noteworthy that those studies did not account for  
595 important vegetation layers for fire management and that GLAS yield products at a  
596 coarser resolution (footprints with diameter of 70 m), despite being a full-waveform  
597 lidar as GEDI. Similarly, by using simulated ICESat-2 photon-counting lidar data,  
598 Narine et al. (2019) models explained 79% of the variation in AGB in a pine-  
599 dominated forest. Gwenzi et al. (2016) described some of the limitations of using  
600 ICESat-2 for retrieving vegetation height in structurally complex savannas. They  
601 found that canopy height estimation in areas of low-density vegetation cover may  
602 have lower precision due to the expected number of signal photons in these areas.  
603 The performance of our models also suggests that GEDI can be more appropriate for  
604 this type of vegetation.

605 Part of the unexplained variance by our  $SS_{fuels}$  models may be due to the lower  
606 sensitivity of GEDI to herbaceous and low stature shrubs compared to the denser

607 overstory tree canopies the GEDI mission was designed to map. GEDI's utility for  
608 mapping short, sparse canopies and understory has yet to be established, and while  
609 the accuracies seen here are likely lower than for closed-canopy forests, or canopy  
610 fuels, our results suggest that GEDI data are still useful for this more challenging  
611 application. The measurement challenge is largely due to convolution of the  
612 waveform return from the ground and from short vegetation above the ground,  
613 where detecting the vegetation from the waveforms will be more challenging. This  
614 issue will be exacerbated over slopes or when vegetation cover is low, which is often  
615 the case in the Cerrado. The top portion of small trees and shrub crowns observed in  
616 the waveforms may not show enough canopy cover to register as a significant return  
617 signal and consequently may not be properly detected using the selected metrics.

618 Although surface, herbaceous and shrub fuels are a key component in fire  
619 behavior and emission models, most previous studies to estimate fuel loads using  
620 spaceborne lidar sensors focused on canopy fuels (García et al., 2012, Peterson et al.,  
621 2013). Obtaining information on fuels in low stature and sparse vegetation  
622 ecosystems, such as savannas and grasslands, is more challenging than in dense  
623 vegetation cover (e.g., Popescu et al., 2018). The lower performance for  $SU_{fuels}$ ,  
624  $HB_{fuels}$ , and  $SH_{fuels}$  suggests that spaceborne lidar data interacts with this lower  
625 stratum less strongly than with tree fuels. In fact, surface components are hardly  
626 directly retrieved with lidar measurements (Jakubowski et al., 2013, Hudak et al.,  
627 2016b, Price and Gordon 2016, Bright et al., 2017), and it is commonly necessary to  
628 rely on their indirect relationship with other variables, such as canopy structure or

629 climate (Hudak et al., 2016a, Mauro et al., 2021). Results in this study demonstrate  
630 that the GEDI waveform metrics could also be used as proxies to indirectly explain  
631 part of the variability of these fuels in savanna ecosystems and underscore the  
632 improvement in modeling  $HB_{fuels}$  and  $SU_{fuels}$  in separate models rather than a single  
633 model ( $SH_{fuels}$ ). The difference among  $HB_{fuels}$  and  $SU_{fuels}$  is indicated by their  
634 contrasting relationships, such as having greater values of  $SU_{fuels}$  in forest  
635 formations (e.g., due to litterfall) and having inverse relationships to CCF and  
636  $HB_{fuels}$ . Nonetheless, the dynamics of  $HB_{fuels}$  and  $SU_{fuels}$  may be more impacted than  
637  $WD_{fuels}$  by plant phenology, seasonality (Costa et al., 2020, Oliveira et al., 2021), and  
638 fire events (Gomes et al., 2020b). Roitman et al. (2018) analyzed decades of AGB  
639 surveys in Cerrado and also demonstrated that environmental factors can help to  
640 explain part of the AGB variation in Cerrado. As more data become available, future  
641 studies could use multitemporal series to exploit the layers' seasonal structural  
642 dynamics mainly due to leaf flush and fall, in search for more unexplained variance  
643 that might not be obtained otherwise. The complementary use of multispectral  
644 and/or hyperspectral images for better distinguishing photosynthetic- from non-  
645 photosynthetic vegetation fractions (e.g., Roberts et a. 2003) coupled to GEDI metrics  
646 might improve the estimation of some surface fuels (e.g., litter, downed wood) in  
647 open-canopy formations and are recommended in future studies.

648 A multilevel approach by linking field plots, UAV-lidar, and spaceborne lidar  
649 data is the backbone of our methodological framework to produce both large scale  
650 multi-layer fuel load information in Cerrado. The RF models developed using

651 simulated GEDI full-waveforms from UAV-lidar have the advantage of not being  
652 affected by waveform geolocation errors that are inherent with GEDI. Currently,  
653 these geolocation errors are around 10-20 m, but are expected to decrease to ~7-8 m  
654 after completed mission calibrations (Dubayah et al., 2020a). This error can make it  
655 difficult to have coincident – in space and time - field and GEDI data for modeling.  
656 Our study is aligned with the simulation approach that has been suitable for GEDI  
657 model development and application (Saarela et al., 2018, Hancock et al., 2019,  
658 Marselis et al., 2019, Patterson et al., 2019, Qi et al., 2019, Schneider et al., 2020,  
659 Dubayah et al., 2020a, Duncanson et al., 2020, Silva et al., 2021). Comprehensive  
660 assessments of the accuracy of on-orbit GEDI data in retrieving key structural  
661 vegetation parameters by synchronizing field measurements within GEDI footprints  
662 may be needed for assessing estimation uncertainty in different scales.  
663 Nevertheless, the models developed with simulated GEDI waveforms can be applied  
664 to the GEDI footprints covering about the entire globe (~52° N and S) providing a  
665 valuable asset for regional to global forest structure analysis as demonstrated for the  
666 Cerrado.

#### 667 **4.2. Caveats and source of uncertainty**

668 While it may be straightforward to derive vegetation structural metrics in  
669 relatively dense vegetation cover (e.g., Popescu et al., 2018), obtaining such  
670 information in low stature and sparse vegetation formations, such as savannas and  
671 grasslands, is more challenging (Glen et al., 2016, Gwenzi et al., 2016). One of the

672 current limitations in our findings concerns the uncertainty of estimating surface and  
673 low stature vegetation fuels. This issue was also described in different studies using  
674 airborne lidar that reported  $R^2$  ranging from ~25 – 45% (Jakubowski et al., 2013,  
675 Hudak et al., 2016b, Price and Gordon 2016, Bright et al., 2017). Pesonen et al. (2008)  
676 models had a better performance for estimating downed dead wood volume in  
677 boreal forests, suggesting a higher predictive capacity for this component.  
678 Nonetheless, despite surface fuels being a key component in fire behavior and  
679 emission models, they have received less attention than canopy fuels, particularly  
680 using spaceborne sensors (Garcia et al., 2012, Peterson et al., 2013, Bright et al., 2017).  
681 Tackling this issue may require inclusion of variables related to fuel dynamics such  
682 as time since the last fire (Chen et al., 2017) and precipitation occurrence (Oliveira et  
683 al., 2021).

684 Another consideration is related to GEDI data characteristics. First, the GEDI  
685 mission is planned to collect data until 2023, limiting application of models to this  
686 time span. Nonetheless, we expect that other missions, such as MOLI (Murooka et al.,  
687 2013, Kimura et al., 2017, Asai et al., 2018), will give similar data in the future. The  
688 second point is related to the sampling nature of GEDI. We observed here that when  
689 aggregating footprints to a 1-km<sup>2</sup> grid cell there were still some areas not yet covered  
690 (Fig. S3), which can be due to the GEDI orbit missing the cells, or data loss from  
691 cloud cover. Those gaps might be filled with forthcoming dataset updates during the  
692 mission; it is expected that most 1 km<sup>2</sup> grid cells will have at least two ground tracks  
693 (Patterson et al., 2019) by the end of the GEDI mission lifetime. The number of



694 required footprints to predict fuel load or AGB density in 1-km<sup>2</sup> cells may vary due  
695 to the vegetation complexity within the cell, which might need further investigation;  
696 nonetheless we observed an exponential decrease in uncertainty with an increase in  
697 number of footprints (Fig S5). Finally, the impact of terrain characteristics for  
698 detecting ground and retrieving waveform metrics was not covered in this study.  
699 When the within footprint terrain slope is high, the interpretation of the signals is  
700 more complex causing, for instance, ground and canopy energy at the same height  
701 (Harding and Carabajal, 2005, Lefsky et al. 2005). In a study comparing small- and  
702 large-footprint lidar sensors, Silva et al. (2018) also observed an effect of terrain slope  
703 (> 20°) by overestimating ground elevation and RH metrics on large-footprint data,  
704 mainly in dense canopies. For instance, an alternative for GLAS waveforms was  
705 applying topographic correction using ancillary data (Lefsky et al., 2005, Lefsky et al.,  
706 2007). Similar effects of topography in the returned GEDI waveform may need to be  
707 investigated and addressed in further studies.

### 708 **4.3 Future Applications and Challenges**

709 Previous studies of GEDI have focused on deriving products by using the  
710 waveform metrics and its relationships with the vertical structure of the vegetation  
711 (Marselis et al., 2019, Schneider et al., 2020, Duncanson et al., 2020). The quality of the  
712 metrics relies on the accuracy to detect the ground signal which is expected to vary  
713 based on various factors such as canopy cover, GEDI beam energy, weather  
714 conditions and topography. However, apart from the environmental characteristics

715 and sensor properties, what determines the ground classification is the algorithm  
716 incorporated. [Hancock et al. \(2019\)](#) described and tested Gaussian fitting along with  
717 the lowest maximum and inflection point algorithms to detect the ground signal and  
718 calculated RH metrics from simulated GEDI waveforms, showing that there might be  
719 differences among them. Further research exploring the impact of ground algorithms  
720 on GEDI metrics associated with fuel load estimation needs to be conducted, ideally  
721 with the study based on individual physiognomies and landscape conditions.

722 RF was implemented in our study due to its ease of usage, interpretability,  
723 versatility in handling missing data, and prior success with respect to fuel load  
724 estimation and to GEDI-based studies ([Healey et al., 2020](#), [Marshak et al., 2020](#),  
725 [Rishmawi et al. 2021](#)). Being an ensemble technique, RF improves the average  
726 prediction performance and is robust to outliers. Techniques such as ordinary least  
727 square regression, lasso logistic regressions and sensitivity analysis, and  
728 combinations of multiple machine learning methods, have also been applied to GEDI  
729 data for quantifying forest traits and structural diversity ([Boucher et al. 2020](#), [Burns](#)  
730 [et al., 2020](#), [Duncanson et al., 2020](#), [Sanchez-Lopez et al., 2020](#)). More recently, deep  
731 learning-based regression models, e.g., Convolutional Neural Networks (CNN), have  
732 been successfully applied for estimating continuous forest structural parameters such  
733 as AGB ([Asner et al., 2018](#)) and canopy height ([Lang et al., 2019](#), [Li et al., 2020](#)). For  
734 instance, [Li et al. \(2020\)](#) showed that deep learning slightly outperforms random  
735 forest models in the estimate of canopy height. Therefore, a review of the efficiency  
736 of various statistical modeling techniques for the estimation of disparate forest

737 metrics can be deemed to be a critical step for furthering GEDI powered research for  
738 fuel load and AGB modeling and management.

739 With several planned global missions, such as NASA-ISRO's NISAR and ESA's  
740 BIOMASS, offering new capabilities, data fusion of GEDI with these distinct sensors  
741 can compensate for drawbacks such as influence of clouds, atmospheric haze,  
742 multiple scattering, sloped terrain and off-nadir pointing ([Pardini et al. 2019](#), [Yang et al., 2011](#), [Quegan et al., 2019](#), [Rosen et al., 2015](#)). We also encourage readers to take  
743 full advantage of the Multi-Mission Algorithm and Analysis Platform (MAAP) that  
744 hosts a colossal amount of related data, tools, algorithms, and computing capabilities  
745 for performing multi-sensor operations ([Albinet et al., 2019](#)). During the initial phase  
746 of GEDI, several studies had explored the possibility of merging GEDI with synthetic  
747 aperture radar (SAR) for improving various forest metrics such as forest height and  
748 other structure attribute mapping and characterization ([Qi et al., 2019](#), [Qi and  
749 Dubayah 2016](#)). Adding to this, a study by [Silva et al. \(2021\)](#) highlighted how  
750 integrating NISAR and ICESat-2 with GEDI offer us new opportunities for enhancing  
751 AGB mapping in temperate forests with complex terrain. Similarly, data from  
752 multispectral sensors also hold potential for improving spatial resolution of GEDI  
753 ([Potapov et al., 2021](#)). Such multi-sensor data fusion approaches will be important for  
754 developing wall-to-wall maps in applications that require higher spatial resolution  
755 such as fire behavior models ([Benali et al., 2016](#), [Saatchi et al., 2007](#)). Data fusion  
756 approaches applicability for estimating large scale forest canopy height, AGB and  
757 past forest disturbances assessment has been already demonstrated ([Potapov et al.,](#)  
758

759 [2021](#), [Saarela et al., 2018](#), [Sanchez-Lopez et al., 2020](#)). Ultimately, data integration  
760 from different missions (e.g., NASA's Landsat 8/OLI and NISAR, and ESA's Sentinel  
761 2/MSI and BIOMASS) will be necessary for developing wall-to-wall maps with finer  
762 spatial resolutions and for covering regions outside GEDI orbit coverage.

763 Fuel mapping is one of the most important stages that should be considered in  
764 wildfire prevention and planning ([Keane and Reeves, 2012](#), [Agee and Skinner, 2005](#);  
765 [Franke et al., 2018](#)). With the proposed framework it is possible to obtain fuel load  
766 estimates for large areas, such as the Cerrado biome. This is a key point for  
767 advancing on a broad spatial scale understanding of fire effects on ecological  
768 processes, ecosystem functioning, carbon emissions, and fuel dynamics ([Turner et al.,](#)  
769 [1995](#), [Bowman et al., 2013](#), [Gomes et al. 2018](#), [Oliveira et al., 2021](#)). Management  
770 solutions based on integrated fire management initiatives have taken place in  
771 Cerrado conservation areas mainly since 2014 and consider practices of prescribed  
772 burning in mosaics to preserve the fire history of a region ([Schmidt et al., 2018](#)). The  
773 fuel components estimate for large areas as developed here will also be an important  
774 resource for this end ([Franke et al., 2018](#), [Gomes et al., 2018](#), [Schmidt et al., 2018](#)).

## 775 **5. Conclusions**

776 In this study we evaluated the capability of GEDI data for estimating large scale  
777 multi-layer fuel loads in a tropical savanna ecosystem. We used the random forest  
778 algorithm fed by GEDI waveform metrics simulated from high-density UAV-lidar  
779 3D point clouds as our modeling approach. To our knowledge, this is the first

780 attempt to map different fuel components with GEDI waveform metrics. Overall, the  
781 models had better performance for predicting woody fuels (e.g.,  $WD_{fuels}$  and  $TF_{fuels}$ ).  
782 Our results support the expected benefits of using GEDI data for improving models  
783 to estimate vegetation traits on structurally-complex ecosystems. Furthermore, we  
784 were able to upscale from local to biome-level predictions by applying our models to  
785 GEDI data over the entire Cerrado yielding relatively high-resolution fuel load  
786 estimates in this region. Therefore, we expect that users can potentially improve  
787 large-scale fuel load monitoring using the presented framework and extend the  
788 analysis to other fire-prone ecosystems. Following research on data integration of  
789 GEDI data with different sensors is expected for meeting spatial and temporal  
790 requirements of other fire-related applications - such as assessing fuel load dynamics,  
791 modeling fire behavior and calculating carbon emissions - and assist in better  
792 understanding the climate-fire interactions across different landscapes.

### 793 **Acknowledgements**

794 This project was supported by the Brazilian National Council for Scientific and  
795 Technological Development (CNPq, grant 442640/2018-8, CNPq/Prevfogo-Ibama N<sup>o</sup>  
796 33/2018). D.R.A.A. was supported by the São Paulo Research Foundation  
797 (#2018/21338-3). This study was financed in part by the Coordenação de  
798 Aperfeiçoamento de Pessoal de Nível Superior – Brasil (CAPES) – Finance Code 001.  
799 A.P.D.C. was financed in part by MCTIC/CNPq N<sup>o</sup> 28/2018 (#408785/2018-7;  
800 #438875/2018-4, #313887/2018-7). V.L., received individual CNPq grant

801 (#315699/2020-5). M.P.F was supported by CNPq grant 306345/2020-0. R.V.L. was  
802 supported by CAPES (#88887.463733/2019-00). We gratefully acknowledge the  
803 following undergraduate and graduate students involved in the field work  
804 campaign: Alberto A. Gontijo e Silva, Alexandre S. C. Filho, André Felipe C. Lima,  
805 Bernardo dos S. de Almeida, Carlos Magno M. de Oliveira, Gilberto do A. Pacheco;  
806 Gustavo R. Lattanzi, Iago Henrique F. da Silva, Irene M. Barbosa, Ivo S. Moreira,  
807 Jacson A. A. Machado, Jean Victor N. Paiva, Junia S. M. Macedo, Leandra Dietrich,  
808 Lídia A. de Aguiar, Matheus Gunther M. Soares, Nelson Amaral, Nivaldo R. J.  
809 Junior, Reginaldo Arthur G. Marcelino, Thiago Trajano, Victor Almeida Cordeiro.  
810 Moreover, we thank the park managers: Edward Elias Junior, Celso Lago-Paiva and  
811 Leandro Chagas from the Serra do Cipó National Park, Maria Carolina A. Camargos  
812 from the Chapada dos Veadeiros National Park and Renato Diniz Dumont from the  
813 Paraopeba National Forest. GatorEye data collection and processing by AMAZ and  
814 ENB was supported in part by the McIntire-Stennis program of the USDA, and the  
815 School of Forest Resources and Conservation and the Center for Latin America  
816 Studies at UFL.

817 **Author Contributions:**

818 R.V.L., C.A.S., and C.K. designed the study. M.B.T.C., A.L.S., L.R.R.Y.G.,  
819 D.R.A.A., G.E.M., A.H., and C.K. collected and processed the field data. E.N.B., and  
820 A.M.A.Z. collected and processed the UAV-lidar data. C.H.A., E.A.T.M. M.M., C.H.,  
821 R.V., B.L.F., C.H.L.S.J., J.L., B.A.F.M., S.H., D.V., and A.C., contributed with the

822 methodological framework, data processing analysis and write up. C.A.S., C.K.,  
823 A.T.H., S.G., D.R.A.A., V.L., A.P.D.C., P.H.S.B, B.A.F.M., L.E.O.C.A., M.G., T.M., S.S.,  
824 S.H., L.D., M.P.F, D.V., and J.X. contributed to the interpretation, quality control and  
825 revisions of the manuscript. All authors read and approved the final version of the  
826 manuscript.

## 827 **References**

- 828 Agee, J. K.; Skinner, C. N. (2005). Basic principles of forest fuel reduction treatments.  
829 *Forest Ecology and Management*, 211(1-2), 83–96.  
830 <https://doi.org/10.1016/j.foreco.2005.01.034>
- 831 Albinet, C., Whitehurst, A. S., Jewell, L. A., Bugbee, K., Laur, H., Murphy, K. J., ... &  
832 Duncanson, L. (2019). A joint ESA-NASA multi-mission algorithm and analysis  
833 platform (MAAP) for biomass, NISAR, and GEDI. *Surveys in Geophysics*, 40(4), 1017-  
834 1027.
- 835 Andela, N., Morton, D.C., Giglio, L., Chen, Y., Van Der Werf, G.R., Kasibhatla, P.S.,  
836 DeFries, R. S., Collatz, G.J., Hantson, S., Kloster, S., Bachelet, D., Forrest, M., Lasslop,  
837 G., Li, F., Mangeon, S., Melton, J. R., Yue, C., Randerson, J. T. (2017). A human-driven  
838 decline in global burned area. *Science*, 356(6354), 1356–1362.  
839 <https://doi.org/10.1126/science.aal4108>
- 840 Andela, N., Morton, D. C., Chen, Y., Giglio, L., Randerson, J. T. (2018). A Global Fire  
841 Atlas of size, duration, and spread from satellite burned area data. In *EGU General*  
842 *Assembly Conference Abstracts* (p. 11269).
- 843 Asai, K., Y. Hirata, G. Takao, H. Simoda, Y. Honda, K. Kajiwara, Y. Awaya. (2018).  
844 “MOLI (Multi-footprintObservation Lidar and Imager) Mission for Globally  
845 Observing Forest Canopy Height and Forest Structural Characteristics from ISS  
846 (International Space Station)-JEM (Japanese Experimental Module).” JpGU Meeting:  
847 Chiba, Japan. May 20- 24.
- 848 Ashworth, A., Evans, D. L., Cooke, W. H., Londo, A., Collins, C., Neuenschwander,  
849 A. (2010). Predicting southeastern forest canopy heights and fire fuel models using  
850 GLAS data. *Photogrammetric Engineering and Remote Sensing*, 76(8), 915-922.
- 851 Asner, G. P., Brodrick, P. G., Philipson, C., Vaughn, N. R., Martin, R. E., Knapp, D. E.,  
852 Heckler, J., Evans, L. J., Jucker, T., Goossens, B., Stark, D. J., Reynolds, G., Ong, R.,

853 Renneboog, N., Kugan, F., Coomes, D. A. (2018). Mapped aboveground carbon  
854 stocks to advance forest conservation and recovery in Malaysian Borneo. *Biological*  
855 *Conservation*, 217, 289–310. <https://doi.org/10.1016/j.biocon.2017.10.020>

856 Beck J., Armston J., Hofton M., Luthcke S. (2020), Global Ecosystem Dynamics  
857 Investigation (GEDI) Level 02 User Guide, Version 1.0.  
858 [https://lpdaac.usgs.gov/documents/650/GEDI02\\_UserGuide\\_V1.pdf](https://lpdaac.usgs.gov/documents/650/GEDI02_UserGuide_V1.pdf) (accessed 13  
859 March 2021)

860 Benali, A.; Ervilha, A. R.; Sá, A. C. L.; Fernandes, P. M.; Pinto, R. M. S.; Trigo, R. M.;  
861 Pereira, J. M. C. (2016). Deciphering the impact of uncertainty on the accuracy of  
862 large wildfire spread simulations. *Science of the Total Environment*, 569, 73–85.  
863 <https://doi.org/10.1016/j.scitotenv.2016.06.112>

864 Blair, J. B., Hofton, M. A. (1999). Modeling laser altimeter return waveforms over  
865 complex vegetation using high-resolution elevation data. *Geophysical research letters*,  
866 26(16), 2509-2512. <https://doi.org/10.1029/1999GL010484>

867 Boucher, P. B., Hancock, S., Orwig, D. A., Duncanson, L., Armston, J., Tang, H., ... &  
868 Schaaf, C. (2020). Detecting change in forest structure with simulated GEDI lidar  
869 waveforms: A case study of the Hemlock Woolly Adelgid (HWA; Adelges tsugae)  
870 infestation. *Remote Sensing*, 12(8), 1304. <https://doi.org/10.3390/rs12081304>

871 Bowman, D. M., O'Brien, J. A., & Goldammer, J. G. (2013). Pyrogeography and the  
872 global quest for sustainable fire management. *Annual Review of Environment and*  
873 *Resources*, 38, 57-80. <https://doi.org/10.1146/annurev-environ-082212-134049>

874 Breiman, L., Friedman, J., Stone, C. J., & Olshen, R. A. (1984). *Classification and*  
875 *regression trees*. CRC press.

876 Breiman, L. (1996). Some properties of splitting criteria. *Machine Learning*, 24(1), 41-  
877 47. <https://doi.org/10.1023/A:1018094028462>

878 Bright, B. C., Hudak, A. T., Meddens, A. J., Hawbaker, T. J., Briggs, J. S., Kennedy, R.  
879 E. (2017). Prediction of forest canopy and surface fuels from lidar and satellite time  
880 series data in a bark beetle-affected forest. *Forests*, 8(9), 322.  
881 <https://doi.org/10.3390/f8090322>

882 Broadbent, E. N., Zambrano, AM. A., Omans, G., Adler, A., Alonso, P., Naylor, D.,  
883 Chenevert, G., Murtha, T., Vogel, J., Almeida, D. R. A., Dalla Corte, A. P., Silva, C. A.,  
884 Prata, G. A., Merrick, T., D'Oliveira, M. V. N., Detto, M., Ferreira, MP., Wilkinson, B.  
885 E., Ferreira, M.E., Muller-Landau, H. C. (2021). In prep. The GatorEye Unmanned  
886 Flying Laboratory: sensor fusion for 4D ecological analysis through custom hardware  
887 and algorithm integration, accessed Feb 10 2021. Retrieved from  
888 <http://www.gatoreye.org>



- 889 Burns, P., Clark, M., Salas, L., Hancock, S., Leland, D., Jantz, P., Goetz, S. J. (2020).  
890 Incorporating canopy structure from simulated GEDI lidar into bird species  
891 distribution models. *Environmental Research Letters*, 15(9), 095002.  
892 <https://doi.org/10.1088/1748-9326/ab80ee>
- 893 Chave, J., Réjou-Méchain, M., Búrquez, A., Chidumayo, E., Colgan, M. S., Delitti, W.  
894 B., ... & Vieilledent, G. (2014). Improved allometric models to estimate the  
895 aboveground biomass of tropical trees. *Global change biology*, 20(10), 3177-3190.  
896 <https://doi.org/10.1111/gcb.12629>
- 897 Chen, L., Yang, J., Kong, H. (2017). Lidar-histogram for fast road and obstacle  
898 detection. In *2017 IEEE International Conference on Robotics and Automation (ICRA)* (pp.  
899 1343-1348). IEEE. <https://doi.org/10.1109/ICRA.2017.7989159>
- 900 Chi, H., Sun, G., Huang, J., Guo, Z., Ni, W., Fu, A. (2015). National Forest  
901 Aboveground Biomass Mapping from ICESat/GLAS Data and MODIS Imagery in  
902 China. *Remote Sensing*, 7(5), 5534-5564. <https://doi.org/10.3390/rs70505534>
- 903 Chuvieco, E., Aguado, I., Salas, J., García, M., Yebra, M., Oliva, P. (2020). Satellite  
904 remote sensing contributions to wildland fire science and management. *Current*  
905 *Forestry Reports*, 6(2), 81-96. <https://doi.org/10.1007/s40725-020-00116-5>
- 906 Chuvieco, E., Aguado, I., Cocero, D., Riano, D. (2003). Design of an empirical index to  
907 estimate fuel moisture content from NOAA-AVHRR images in forest fire danger  
908 studies. *International Journal of Remote Sensing*, 24(8), 1621-1637.  
909 <https://doi.org/10.1080/01431160210144660b>
- 910 Costa, M.B.T. da, Silva, C.A., Broadbent, E.N., Leite, R.V., Mohan, M., Liesenberg, V.,  
911 Stoddart, J., Amaral, C.H. do, Almeida, D.R.A. de, Silva, A.L. da, Goya, L.R.R.Y.,  
912 Cordeiro, V.A., Rex, F., Hirsch, A., Marcatti, G.E., Cardil, A., Mendonça, B.A.F. de,  
913 Hamamura, C., Dalla Corte, A.P., Matricardi, E.A.T., Hudak, A.T., Zambrano,  
914 A.M.A., Valbuena, R., Faria, B.L. de, Junior, C.H.L.S., Aragão, L., Ferreira, M.E.,  
915 Liang, J., Carvalho, S. de P.C. e, Klauberg, C., (2021). Beyond trees: Mapping total  
916 aboveground biomass density in the Brazilian savanna using high-density UAV-lidar  
917 data. *Forest Ecology and Management* 491.  
918 <https://doi.org/https://doi.org/10.1016/j.foreco.2021.119155>
- 919 Costa, A.N., Souza, J.R., Alves, K.M., Penna-Oliveira, A., Paula-Silva, G., Becker, I.S.,  
920 Marinho-Vieira, K., Bonfim, A.L., Bartimachi, A., Vieira-Neto, E.H.M.(2020). Linking  
921 the spatiotemporal variation of litterfall to standing vegetation biomass in Brazilian  
922 savannas. *Journal of Plant Ecology*. 13, 517–524. <https://doi.org/10.1093/jpe/rtaa039>
- 923 Dubayah, R., Blair, J. B., Goetz, S., Fatoyinbo, L., Hansen, M., Healey, S., Hofton, M.,  
924 Hurtt, G., Kellner, J., Luthcke, S., Armston, J., Tang, H., Duncanson, L., Hancock, S.,  
925 Jantz, P., Marselis, S., Patterson, P. L., Qi, W., Silva, C. (2020a). The Global Ecosystem

926 Dynamics Investigation: High-resolution laser ranging of the Earth's forests and  
927 topography. *Science of Remote Sensing*, 1, 100002.  
928 <https://doi.org/10.1016/j.srs.2020.100002>

929 [dataset] Dubayah, R., M. Hofton, J. Blair, J. Armston, H. Tang, S. Luthcke. GEDI L2A  
930 Elevation and Height Metrics Data Global Footprint Level V002. 2021, distributed by  
931 NASA EOSDIS Land Processes DAAC, [https://doi.org/10.5067/GEDI/GEDI02\\_A.002](https://doi.org/10.5067/GEDI/GEDI02_A.002).  
932 Accessed 2021-08-29.

933 [dataset] Dubayah, R., H. Tang, J. Armston, S. Luthcke, M. Hofton, J. Blair. GEDI L2B  
934 Canopy Cover and Vertical Profile Metrics Data Global Footprint Level V002. 2021,  
935 distributed by NASA EOSDIS Land Processes DAAC,  
936 [https://doi.org/10.5067/GEDI/GEDI02\\_B.002](https://doi.org/10.5067/GEDI/GEDI02_B.002). Accessed 2021-08-29.

937 Duncanson, L., Neuenschwander, A., Hancock, S., Thomas, N., Fatoyinbo, T.,  
938 Simard, M., Dubayah, R. (2020). Biomass estimation from simulated GEDI, ICESat-2  
939 and NISAR across environmental gradients in Sonoma County, California. *Remote*  
940 *Sensing of Environment*, 242, 111779. <https://doi.org/10.1016/j.rse.2020.111779>

941 Duncanson, L. I., Niemann, K. O., Wulder, M. A. (2010). Estimating forest canopy  
942 height and terrain relief from GLAS waveform metrics. *Remote Sensing of*  
943 *Environment*, 114(1), 138-154. <https://doi.org/10.1016/j.rse.2009.08.018>

944 Durigan, G., Ratter, J. A. (2016). The need for a consistent fire policy for Cerrado  
945 conservation. *Journal of Applied Ecology*, 53(1), 11-15. [https://doi.org/10.1111/1365-](https://doi.org/10.1111/1365-2664.12559)  
946 [2664.12559](https://doi.org/10.1111/1365-2664.12559)

947 Durigan, G., Pilon, N. A., Abreu, R. C., Hoffmann, W. A., Martins, M., Fiorillo, B. F.,  
948 Vasconcelos, H. L. (2020). No net loss of species diversity after prescribed fires in the  
949 Brazilian Savanna. *Frontiers in Forests and Global Change*, 3, 13.  
950 <https://doi.org/10.3389/ffgc.2020.00013>

951 Erdody, T. L., Moskal, L. M. (2010). Fusion of LiDAR and imagery for estimating  
952 forest canopy fuels. *Remote Sensing of Environment*, 114(4), 725-737.  
953 <https://doi.org/10.1016/j.rse.2009.11.002>

954 Ferreira, L.G., Urban, T.J., Neuenschawander, A., De Araújo, F.M. (2011). Use of  
955 Orbital LIDAR in the Brazilian Cerrado Biome: Potential Applications and Data  
956 Availability. *Remote Sensing*, 3(10), 2187-2206. <https://doi.org/10.3390/rs3102187>

957 Franke, J., Barradas, A. C. S., Borges, M. A., Menezes Costa, M., Dias, P. A.,  
958 Hoffmann, A. A., Orozco Filho, J. C., Melchiori, A. E., Siegert, F. (2018). Fuel load  
959 mapping in the Brazilian Cerrado in support of integrated fire management. *Remote*  
960 *Sensing of Environment*, 217, 221–232. <https://doi.org/10.1016/j.rse.2018.08.018>

- 961 Gajardo, J., García, M., & Riaño, D. (2014). Applications of Airborne Laser Scanning  
 962 in Forest Fuel Assessment and Fire Prevention. In M. Maltamo, E. Næsset, & J.  
 963 Vauhkonen (Eds.), *Forestry Applications of Airborne Laser Scanning: Concepts and*  
 964 *Case Studies* (pp. 439-462). Dordrecht: Springer Netherlands
- 965 García, M., Popescu, S., Riaño, D., Zhao, K., Neuenschwander, A., Agca, M.,  
 966 Chuvieco, E. (2012). Characterization of canopy fuels using ICESat/GLAS data.  
 967 *Remote Sensing of Environment*, 123, 81-89. <https://doi.org/10.1016/j.rse.2012.03.018>
- 968 García, M., Saatchi, S., Casas, A., Koltunov, A., Ustin, S.L., Ramirez, C., Balzter, H.  
 969 (2017). Extrapolating forest canopy fuel properties in the California Rim fire by  
 970 combining airborne LiDAR and landsat OLI data. *Remote Sensing* 9, 1–18.  
 971 <https://doi.org/10.3390/rs9040394>
- 972 Glenn, N. F., Neuenschwander, A., Vierling, L. A., Spaete, L., Li, A., Shinneman, D. J.,  
 973 McIlroy, S. K. (2016). Landsat 8 and ICESat-2: Performance and potential synergies  
 974 for quantifying dryland ecosystem vegetation cover and biomass. *Remote Sensing of*  
 975 *Environment*, 185, 233–242. <http://dx.doi.org/10.1016/j.rse.2016.02.039>
- 976 Gomes, L., Miranda, H. S., Silvério, D. V., Bustamante, M. M. C. (2020a). Effects and  
 977 behaviour of experimental fires in grasslands, savannas, and forests of the Brazilian  
 978 Cerrado. *Forest Ecology and Management*, 458, 117804.  
 979 <https://doi.org/10.1016/j.foreco.2019.117804>
- 980 Gomes, L., Miranda, H.S., Soares-Filho, B., Rodrigues, L., Oliveira, U., Bustamante,  
 981 M.M.C., (2020b). Responses of Plant Biomass in the Brazilian Savanna to Frequent  
 982 Fires. *Frontiers in Forests and Global Change* 3, 1–11.  
 983 <https://doi.org/10.3389/ffgc.2020.507710>
- 984 Gomes, L., Miranda, H. S., Bustamante, M. M. da C. (2018). How can we advance the  
 985 knowledge on the behavior and effects of fire in the Cerrado biome?. *Forest Ecology*  
 986 *and Management*, 417, 281–290. <https://doi.org/10.1016/j.foreco.2018.02.032>
- 987 Gwenz, D., Lefsky, M. A., Suchdeo, V. P., Harding, D. J. (2016). Prospects of the  
 988 ICESat-2 laser altimetry mission for savanna ecosystem structural studies based on  
 989 airborne simulation data. *ISPRS Journal of Photogrammetry and Remote Sensing*, 118, 68-  
 990 82. <https://doi.org/10.1016/j.isprsjprs.2016.04.009>
- 991 Hall, F. G., Bergen, K., Blair, J. B., Dubayah, R., Houghton, R., Hurtt, G., ... &  
 992 Wickland, D. (2011). Characterizing 3D vegetation structure from space: Mission  
 993 requirements. *Remote Sensing of Environment*, 115(11), 2753-2775.
- 994 Hancock, S., Armston, J., Hofton, M., Sun, X., Tang, H., Duncanson, L. I., Dubayah, R.  
 995 (2019). The GEDI simulator: A large-footprint waveform lidar simulator for

- 996 calibration and validation of spaceborne missions. *Earth and Space Science*, 6(2), 294-  
997 310. <https://doi.org/10.1029/2018EA000506>
- 998 Hantson, S., Pueyo, S., Chuvieco, E. (2015). Global fire size distribution is driven by  
999 human impact and climate. *Global Ecology and Biogeography*, 24(1), 77-86.  
1000 <https://doi.org/10.1111/geb.12246>
- 1001 Harding, D. J., Carabajal, C. C. (2005). ICESat waveform measurements of within-  
1002 footprint topographic relief and vegetation vertical structure. *Geophysical research*  
1003 *letters*, 32(21), 4. <https://doi.org/10.1029/2005GL023471>
- 1004 Healey, S. P., Yang, Z., Gorelick, N., Ilyushchenko, S. (2020). Highly Local Model  
1005 Calibration with a New GEDI LiDAR Asset on Google Earth Engine Reduces Landsat  
1006 Forest Height Signal Saturation. *Remote Sensing*, 12(17), 2840.  
1007 <https://doi.org/10.3390/rs12172840>
- 1008 Hermosilla, T., Coops, N. C., Ruiz, L. A., Moskal, L. M. (2014). Deriving pseudo-  
1009 vertical waveforms from small-footprint full-waveform LiDAR data. *Remote sensing*  
1010 *letters*, 5(4), 332-341. <https://doi.org/10.1080/2150704X.2014.903350>
- 1011 Hoffmann, W. A., Jaconis, S. Y., McKinley, K. L., Geiger, E. L., Gotsch, S. G., &  
1012 Franco, A. C. (2012). Fuels or microclimate? Understanding the drivers of fire  
1013 feedbacks at savanna-forest boundaries. *Austral Ecology*, 37(6), 634-643.  
1014 <https://doi.org/10.1111/j.1442-9993.2011.02324.x>
- 1015 Hofton M., and Blair J.B. (2019) Algorithm Theoretical Basis Document (ATBD) for  
1016 GEDI Transmit and Receive Waveform Processing for L1 and L2 Products.  
1017 [https://lpdaac.usgs.gov/documents/581/GEDI\\_WF\\_ATBD\\_v1.0.pdf](https://lpdaac.usgs.gov/documents/581/GEDI_WF_ATBD_v1.0.pdf). (accessed 13  
1018 March 2021)
- 1019 Hu, T., Ma, Q., Su, Y., Battles, J.J., Collins, B. M., Stephens, S. L., Kelly, M., Guo, Q.  
1020 (2019). A simple and integrated approach for fire severity assessment using bi-  
1021 temporal airborne LiDAR data. *International Journal of Applied Earth Observation and*  
1022 *Geoinformation*, 78, 25-38. <https://doi.org/10.1016/j.jag.2019.01.007>
- 1023 Hudak, A. T., Bright, B. C., Pokswinski, S. M., Loudermilk, E. L., O'Brien, J. J.,  
1024 Hornsby, B. S., Silva, C. A. (2016a). Mapping forest structure and composition from  
1025 low-density LiDAR for informed forest, fuel, and fire management at Eglin Air Force  
1026 Base, Florida, USA. *Canadian Journal of Remote Sensing*, 42(5), 411-427.  
1027 <https://doi.org/10.1080/07038992.2016.1217482>
- 1028 Hudak, A. T., Dickinson, M. B., Bright, B. C., Kremens, R. L., Loudermilk, E. L.,  
1029 O'Brien, J. J., Ottmar, R. D. (2016b). Measurements relating fire radiative energy  
1030 density and surface fuel consumption-RxCADRE 2011 and 2012. *International Journal*  
1031 *of Wildland Fire*, 25(1), 25-37. <https://doi.org/10.1080/07038992.2016.1217482>

1032

1033 Jakubowski, M. K., Guo, K., Collins, B., Stephens, S., Kelly, M. (2013). Predicting  
1034 Surface Fuel Models and Fuel Metrics Using Lidar and CIR Imagery in a Dense,  
1035 Mountainous Forest. *Photogrammetric Engineering & Remote Sensing*, 79(1), 37–49.  
1036 <https://doi.org/10.14358/PERS.79.1.37>

1037 Keane, R. E., Herynk, J. M., Toney, C., Urbanski, S. P., Lutes, D. C., Ottmar, R. D.  
1038 (2013). Evaluating the performance and mapping of three fuel classification systems  
1039 using Forest Inventory and Analysis surface fuel measurements. *Forest Ecology and*  
1040 *Management*, 305, 248–263. <https://doi.org/10.1016/j.foreco.2013.06.001>

1041 Keane, R. E., Reeves, M. (2012). Use of Expert Knowledge to Develop Fuel Maps for  
1042 Wildland Fire Management. A. H. Perera et al. (eds.), *Expert Knowledge and Its*  
1043 *Application in Landscape Ecology*. Springer. (pp 211-228).  
1044 [https://doi.org/10.1007/978-1-4614-1034-8\\_11](https://doi.org/10.1007/978-1-4614-1034-8_11).

1045 Kimura, T., Imai, T., Sakaizawa, D., Murooka, J., Mitsunashi, R. (2017). The overview  
1046 and status of vegetation Lidar mission, MOLI. In *2017 IEEE International Geoscience*  
1047 *and Remote Sensing Symposium (IGARSS)* (pp. 4228-4230). IEEE.  
1048 <https://doi.org/10.1109/IGARSS.2017.8127935>

1049 Klauber, C., Hudak, A. T., Silva, C. A., Lewis, S. A., Robichaud, P. R., Jain, T. B.  
1050 (2019). Characterizing fire effects on conifers at tree level from airborne laser  
1051 scanning and high-resolution, multispectral satellite data. *Ecological Modelling*, 412,  
1052 108820. <https://doi.org/10.1016/j.ecolmodel.2019.108820>

1053

1054 Kuhn, M., Wing, J., Weston, S., Williams, A., Keefer, C., Engelhardt, A., Benesty, M.  
1055 (2020). Package ‘caret’. *The R Journal*, 223.

1056 Lang, N., Schindler, K., Wegner, J. D. (2019). Country-Wide High-Resolution  
1057 Vegetation Height Mapping with Sentinel-2. *Remote Sensing of Environment*, 233,  
1058 111347. <http://doi.org/10.1016/j.rse.2019.111347>

1059 Lê, S., Josse, J., Husson, F. (2008). FactoMineR: an R package for multivariate  
1060 analysis. *Journal of statistical software*, 25(1), 1-18.

1061 Lefsky, M. A., Keller, M., Pang, Y., De Camargo, P. B., Hunter, M. O. (2007). Revised  
1062 method for forest canopy height estimation from Geoscience Laser Altimeter System  
1063 waveforms. *Journal of Applied Remote Sensing*, 1(1), 013537.  
1064 <https://doi.org/10.1117/1.2795724>

1065 Lefsky, M. A., Harding, D. J., Keller, M., Cohen, W. B., Carabajal, C. C., Espirito-  
1066 Santo, F. D., ... & de Camargo, P. B. (2006). Correction to “Estimates of forest canopy

1067 height and aboveground biomass using ICESat". *Geophysical Research Letters*, 32(5),  
1068 L05501. <https://doi.org/10.1029/2005GL025518>.

1069 Lefsky, M. A., Harding, D. J., Keller, M., Cohen, W. B., Carabajal, C. C., Espirito-  
1070 Santo, F. D., (2005). Estimates of forest canopy height and aboveground biomass  
1071 using ICESat. *Geophysical research letters*, 32(22). <https://doi.org/10.1029/2005GL023971>

1072 Lehmann, C.E.R., Anderson, T.M., Sankaran, M., Higgins, S.I., Archibald, S.,  
1073 Hoffmann, W.A., Hanan, N.P., Williams, R.J., Fensham, R.J., Felfili, J., Hutley, L.B.,  
1074 Ratnam, J., San Jose, J., Montes, R., Franklin, D., Russell-Smith, J., Ryan, C.M.,  
1075 Durigan, G., Hiernaux, P., Haidar, R., Bowman, D.M.J.S., Bond, W.J., (2014). Savanna  
1076 vegetation-fire-climate relationships differ among continents. *Science* 343, 548–552.  
1077 <https://doi.org/10.1126/science.1247355>

1078 Li,W., Niu, Z., Shang, R., Qin, Y., Wang, L., Chen, H. (2020). High-Resolution  
1079 Mapping of Forest Canopy Height Using Machine Learning by Coupling ICESat-2  
1080 LiDAR with Sentinel-1, Sentinel-2 and Landsat-8 Data. *International Journal of Applied*  
1081 *Earth Observation and Geoinformation*, 92, 102163.  
1082 <https://doi.org/10.1016/j.jag.2020.102163>

1083 MacArthur, R. H., & Horn, H. S. (1969). Foliage profile by vertical measurements.  
1084 *Ecology*, 50(5), 802-804. <https://doi.org/10.2307/1933693>

1085

1086 Marselis, S. M., Tang, H., Armston, J., Abernethy, K., Alonso, A., Barbier, N., ... &  
1087 Dubayah, R. (2019). Exploring the relation between remotely sensed vertical canopy  
1088 structure and tree species diversity in Gabon. *Environmental Research Letters*, 14(9),  
1089 094013.

1090 Marselis, S. M., Tang, H., Armston, J. D., Calders, K., Labrière, N., Dubayah, R.  
1091 (2018). Distinguishing vegetation types with airborne waveform lidar data in a  
1092 tropical forest-savanna mosaic: A case study in Lopé National Park, Gabon. *Remote*  
1093 *sensing of environment*, 216, 626-634.

1094 Marshak, C., Simard, M., Duncanson, L., Silva, C. A., Denbina, M., Liao, T. H., ... &  
1095 Armston, J. (2020). Regional Tropical Aboveground Biomass Mapping with L-Band  
1096 Repeat-Pass Interferometric Radar, Sparse Lidar, and Multiscale Superpixels. *Remote*  
1097 *Sensing*, 12(12), 2048. <https://doi.org/10.3390/rs12122048>

1098 Mauro, F., Hudak, A. T., Fekety, P. A., Frank, B., Temesgen, H., Bell, D. M., ... &  
1099 McCarley, T. R. (2021). Regional Modeling of Forest Fuels and Structural Attributes  
1100 Using Airborne Laser Scanning Data in Oregon. *Remote Sensing*, 13(2), 261.  
1101 <https://doi.org/10.3390/rs13020261>

- 1102 Murooka, J., Kobayashi, T., Imai, T., Suzuki, K., Sakaizawa, D., Yamakawa, S., ... &  
1103 Asai, K. (2013). Overview of Japan's spaceborne vegetation lidar mission. In *Lidar*  
1104 *Technologies, Techniques, and Measurements for Atmospheric Remote Sensing IX* (Vol.  
1105 8894, p. 88940B). International Society for Optics and Photonics.
- 1106 Myers, N., Mittermeier, R. A., Mittermeier, C. G., Da Fonseca, G. A., & Kent, J. (2000).  
1107 Biodiversity hotspots for conservation priorities. *Nature*, 403(6772), 853-858.  
1108 <https://doi.org/10.1117/12.2029119>
- 1109 Narine, L. L., Popescu, S. C., & Malambo, L. (2020). Using ICESat-2 to estimate and  
1110 map forest aboveground biomass: A first example. *Remote Sensing*, 12(11), 1824.
- 1111 Narine, L. L., Popescu, S., Neuenschwander, A., Zhou, T., Srinivasan, S., Harbeck, K.  
1112 (2019). Estimating aboveground biomass and forest canopy cover with simulated  
1113 ICESat-2 data. *Remote Sensing of Environment*, 224, 1–11.  
1114 <https://doi.org/10.1016/j.rse.2019.01.037>
- 1115 Ogle, S. M., Kurz, W. A., Green, C., Brandon, A., Baldock, J., Domke, G., Herold, M.,  
1116 Bernoux, M., ... & Waterworth, R. M. (2019). Chapter 2: Generic Methodologies  
1117 Applicable To Multiple Land-Use Categories. 2019 Refinement to the 2006 IPCC  
1118 Guidelines for National Greenhouse Gas Inventories 1–59.
- 1119 Oliveira, U., Soares-Filho, B., de Souza Costa, W.L., Gomes, L., Bustamante, M.,  
1120 Miranda, H., (2021). Modeling fuel loads dynamics and fire spread probability in the  
1121 Brazilian Cerrado. *Forest Ecology and Management* 482.  
1122 <https://doi.org/10.1016/j.foreco.2020.118889>
- 1123 Pardini, M., Armston, J., Qi, W., Lee, S. K., Tello, M., Bes, V. C., ... & Fatoyinbo, L. E.  
1124 (2019). Early lessons on combining lidar and multi-baseline SAR measurements for  
1125 forest structure characterization. *Surveys in Geophysics*, 40(4), 803-837.  
1126 <https://doi.org/10.1007/s10712-019-09553-9>
- 1127 Patterson, P. L., Healey, S. P., Ståhl, G., Saarela, S., Holm, S., Andersen, H. E., ... &  
1128 Yang, Z. (2019). Statistical properties of hybrid estimators proposed for GEDI—  
1129 NASA's global ecosystem dynamics investigation. *Environmental Research Letters*,  
1130 14(6), 065007. <https://doi.org/10.1088/1748-9326/ab18df>
- 1131 Pesonen, A., Maltamo, M., Eerikäinen, K., Packalèn, P. (2008). Airborne laser  
1132 scanning-based prediction of coarse woody debris volumes in a conservation area.  
1133 *Forest Ecology and Management*, 255(8-9), 3288-3296.  
1134 <https://doi.org/10.1016/j.foreco.2008.02.017>
- 1135 Peterson, B., Nelson, K., & Wylie, B. (2013). Towards integration of GLAS into a  
1136 national fuel mapping program. *Photogrammetric Engineering & Remote Sensing*, 79(2),  
1137 175-183. <https://doi.org/10.14358/PERS.79.2.175>

1138

1139 Popescu, S. C.; Zhou, T.; Nelson, R.; Neuenschwander, A.; Sheridan, R.; Narine, L.;  
1140 Walsh, K. M. (2018). Photon counting LiDAR: An adaptive ground and canopy  
1141 height retrieval algorithm for ICESat-2 data. *Remote Sensing of Environment*, 208, 154–  
1142 170. <https://doi.org/10.1016/j.rse.2018.02.019>

1143 Popescu, S. C., Zhao, K., Neuenschwander, A., Lin, C. (2011). Satellite lidar vs. small  
1144 footprint airborne lidar: Comparing the accuracy of aboveground biomass estimates  
1145 and forest structure metrics at footprint level. *Remote Sensing of Environment*, 115(11),  
1146 2786–2797. <https://doi.org/10.1016/j.rse.2011.01.026>

1147 Potapov, P., Li, X., Hernandez-Serna, A., Tyukavina, A., Hansen, M. C.,  
1148 Kommareddy, A., ... & Hofton, M. (2021). Mapping global forest canopy height  
1149 through integration of GEDI and Landsat data. *Remote Sensing of Environment*, 253,  
1150 112165. <https://doi.org/10.1016/j.rse.2020.1121>

1151 Price, O. F., Gordon, C. E. (2016). The potential for LiDAR technology to map fire fuel  
1152 hazard over large areas of Australian forest. *Journal of Environmental Management*,  
1153 181, 663-673. <http://dx.doi.org/10.1016/j.jenvman.2016.08.042>

1154 Qi, W., Dubayah, R. O. (2016). Combining Tandem-X InSAR and simulated GEDI  
1155 lidar observations for forest structure mapping. *Remote Sensing of Environment*,  
1156 187, 253-266. <https://doi.org/10.1016/j.rse.2016.10.018>

1157 Qi, W., Lee, S. K., Hancock, S., Luthcke, S., Tang, H., Armston, J., Dubayah, R. (2019).  
1158 Improved forest height estimation by fusion of simulated GEDI Lidar data and  
1159 TanDEM-X InSAR data. *Remote sensing of environment*, 221, 621-634.  
1160 <https://doi.org/10.1016/j.rse.2018.11.035>

1161 Quegan, S., Le Toan, T., Chave, J., Dall, J., Exbrayat, J. F., Minh, D. H. T., ... &  
1162 Williams, M. (2019). The European Space Agency BIOMASS mission: Measuring  
1163 forest above-ground biomass from space. *Remote Sensing of Environment*, 227, 44-60.  
1164 <https://doi.org/10.1016/j.rse.2019.03.032>

1165 R Core Team. (2020). R: A Language and Environment for Statistical Computing. R  
1166 Foundation for Statistical Computing. Vienna, Austria. <https://www.R-project.org/>.  
1167 (accessed 13 March 2021)

1168 Rishmawi, K., Huang, C., & Zhan, X. (2021). Monitoring Key Forest Structure  
1169 Attributes across the Conterminous United States by Integrating GEDI LiDAR  
1170 Measurements and VIIRS Data. *Remote Sensing*, 13(3), 442.  
1171 <https://doi.org/10.3390/rs13030442>



- 1172 Roberts, D.A., Dennison, P.E., Gardner, M.E., Hetzel, Y., Ustin, S.L., Lee, C.T. (2003).  
1173 Evaluation of the potential of Hyperion for fire danger assessment by comparison to  
1174 the airborne visible/infrared imaging spectrometer. *IEEE Transactions on Geoscience*  
1175 *and Remote Sensing* 41, 1297–1310. <https://doi.org/10.1109/TGRS.2003.812904>
- 1176 Roitman, I., Bustamante, M.M.C., Haidar, R.F., Shimbo, J.Z., Abdala, G.C., Eiten, G.,  
1177 Fagg, C.W., Felfili, M.C., Felfili, J.M., Jacobson, T.K.B., Lindoso, G.S., Keller, M.,  
1178 Lenza, E., Miranda, S.C., Pinto, J.R.R., Rodrigues, A.A., Delitti, W.B.C., Roitman, P.,  
1179 Sampaio, J.M., 2018. Optimizing biomass estimates of savanna woodland at different  
1180 spatial scales in the Brazilian Cerrado: Re-evaluating allometric equations and  
1181 environmental influences. *PLoS ONE* 13, 1–21.  
1182 <https://doi.org/10.1371/journal.pone.0196742>
- 1183 Rosan, T. M., Aragão, L. E., Oliveras, I., Phillips, O. L., Malhi, Y., Gloor, E., &  
1184 Wagner, F. H. (2019). Extensive 21st-century woody encroachment in South  
1185 America's savanna. *Geophysical Research Letters*, 46(12), 6594-6603.
- 1186 Rosen, P. A., Hensley, S., Shaffer, S., Veilleux, L., Chakraborty, M., Misra, T., ... &  
1187 Satish, R. (2015, May). The NASA-ISRO SAR mission-An international space  
1188 partnership for science and societal benefit. In *2015 IEEE Radar Conference (RadarCon)*  
1189 (pp. 1610-1613). IEEE.
- 1190 Saarela, S., Holm, S., Healey, S. P., Andersen, H. E., Petersson, H., Prentius, W., ... &  
1191 Ståhl, G. (2018). Generalized hierarchical model-based estimation for aboveground  
1192 biomass assessment using GEDI and Landsat data. *Remote Sensing*, 10(11) 1832.  
1193 <https://doi.org/10.3390/rs10111832>
- 1194 Saatchi, S.; Halligan, K.; Despain, D. G.; Crabtree, R. L. Estimation of forest fuel load  
1195 from radar remote sensing (2007). *IEEE Transactions on Geoscience and Remote Sensing*,  
1196 45(6), 1726–1740. <https://doi.org/10.1109/TGRS.2006.887002>.
- 1197 Sanchez-Lopez, N., Boschetti, L., Hudak, A. T., Hancock, S., Duncanson, L. I. (2020).  
1198 Estimating Time Since the Last Stand-Replacing Disturbance (TSD) from Spaceborne  
1199 Simulated GEDI Data: A Feasibility Study. *Remote Sensing*, 12(21), 3506.  
1200 <https://doi.org/10.3390/rs12213506>
- 1201 Sandberg, D. V., Ottmar, R. D., & Cushon, G. H. (2001). Characterizing fuels in the  
1202 21st century. *International Journal of Wildland Fire*, 10(4), 381-387.  
1203 <https://doi.org/10.1071/WF01036>
- 1204 Schmidt, I. B., Moura, L. C., Ferreira, M. C., Eloy, L., Sampaio, A. B., Dias, P. A., &  
1205 Berlinck, C. N. (2018). Fire management in the Brazilian savanna: First steps and the  
1206 way forward. *Journal of applied ecology*, 55(5), 2094-2101.  
1207 <https://doi.org/10.1111/1365-2664.13118>

- 1208 Schneider, F. D., Ferraz, A., Hancock, S., Duncanson, L. I., Dubayah, R. O., Pavlick, R.  
1209 P., Schimel, D. S. (2020). Towards mapping the diversity of canopy structure from  
1210 space with GEDI. *Environmental Research Letters*, 15(11), 115006.  
1211 <https://doi.org/10.5068/D16T06>
- 1212 Silva, C.A., Duncanson, L., Hancock, S., Neuenschwander, A., Thomas, N., Hofton,  
1213 M., Fatoyinbo, L., Simard, M., Marshak, C.Z., Armston, J., Lutchke, S., Dubayah, R.,  
1214 (2021). Fusing simulated GEDI, ICESat-2 and NISAR data for regional aboveground  
1215 biomass mapping. *Remote Sensing of Environment* 253.  
1216 <https://doi.org/10.1016/j.rse.2020.112234>
- 1217 Silva, C. A., Hamamura, C., Valbuena, R., Hancock, S., Cardil, A., Broadbent, E. N.,  
1218 Almeida, D. R. A., Silva Junior, C. H. L., Klauber, C. (2020). rGEDI: NASA's Global  
1219 Ecosystem Dynamics Investigation (GEDI) Data Visualization and Processing.  
1220 version 0.1.8, accessed on October. 22 2020, available at: [https://CRAN.R-](https://CRAN.R-project.org/package=rGEDI)  
1221 [project.org/package=rGEDI](https://CRAN.R-project.org/package=rGEDI)
- 1222 Silva, C. A., Saatchi, S., Garcia, M., Labriere, N., Klauber, C., Ferraz, A., ... & Hudak,  
1223 A. T. (2018). Comparison of small-and large-footprint lidar characterization of  
1224 tropical forest aboveground structure and biomass: A case study from central gabon.  
1225 *IEEE Journal of Selected Topics in Applied Earth Observations and Remote Sensing*, 11(10),  
1226 3512-3526. <https://doi.org/10.1109/JSTARS.2018.2816962>
- 1227 Simon, M.F.; Grether, R.; Queiroz, L.P.; Skema, C.; Pennington, R.T. Hughes, C. E.  
1228 (2009). Recent assembly of the Cerrado, a Neotropical plant diversity hotspot, by in  
1229 situ evolution of adaptations to fire. *Proceedings of the National Academy of Science*  
1230 *USA*, 106(48): 20359-20364. <https://doi.org/10.1073/pnas.0903410106>
- 1231 Souza, C.M., Shimbo, J.Z., Rosa, M.R., Parente, L.L., Alencar, A.A., Rudorff, B.F.T.,  
1232 Hasenack, H., Matsumoto, M., Ferreira, L.G., Souza-Filho, P.W.M., de Oliveira, S.W.,  
1233 Rocha, W.F., Fonseca, A. V., Marques, C.B., Diniz, C.G., Costa, D., Monteiro, D., Rosa,  
1234 E.R., Vélez-Martin, E., Weber, E.J., Lenti, F.E.B., Paternost, F.F., Pareyn, F.G.C.,  
1235 Siqueira, J. V., Viera, J.L., Neto, L.C.F., Saraiva, M.M., Sales, M.H., Salgado, M.P.G.,  
1236 Vasconcelos, R., Galano, S., Mesquita, V. V., Azevedo, T. (2020). Reconstructing three  
1237 decades of land use and land cover changes in brazilian biomes with landsat archive  
1238 and earth engine. *Remote Sensing* 12. <https://doi.org/10.3390/RS12172735>
- 1239 Stavros, E. N., Coen, J., Peterson, B., Singh, H., Kennedy, K., Ramirez, C., Schimel, D.  
1240 (2018). Use of imaging spectroscopy and LIDAR to characterize fuels for fire  
1241 behavior prediction. *Remote Sensing Applications: Society and Environment*, 11, 41–50.  
1242 <https://doi.org/10.1016/j.rsase.2018.04.010>
- 1243 Stefanidou, A., Gitas, I. Z., Korhonen, L., Stavrakoudis, D., & Georgopoulos, N.  
1244 (2020). LiDAR-based estimates of canopy base height for a dense uneven-aged  
1245 structured forest. *Remote Sensing*, 12(10), 1565. <https://doi.org/10.3390/rs12101565>

- 1246 Strassburg, B. B., Brooks, T., Feltran-Barbieri, R., Iribarrem, A., Crouzeilles, R.,  
1247 Loyola, R., ... & Balmford, A. (2017). Moment of truth for the Cerrado hotspot. *Nature*  
1248 *Ecology & Evolution*, 1(4), 1-3. <https://doi.org/10.1038/s41559-017-0099>
- 1249 Szpakowski, D. M., Jensen, J. L. (2019). A review of the applications of remote  
1250 sensing in fire ecology. *Remote Sensing*, 11(22), 2638.  
1251 <https://doi.org/10.3390/rs11222638>
- 1252 Tang, H., Armston, J. (2019). Algorithm Theoretical Basis Document (ATBD) for  
1253 GEDI L2B Footprint Canopy Cover and Vertical Profile Metrics.  
1254 [https://lpdaac.usgs.gov/documents/588/GEDI\\_FCCVPM\\_ATBD\\_v1.0.pdf](https://lpdaac.usgs.gov/documents/588/GEDI_FCCVPM_ATBD_v1.0.pdf). (accessed  
1255 13 March 2021)
- 1256 Turner, M. G., Gardner, R. H., & O'neill, R. V. (1995). Ecological dynamics at broad  
1257 scales. *BioScience*, 45, S29-S35.
- 1258 Wulder, M.A., White, J.C., Nelson, R.F., Næsset, E., Ørka, H.O., Coops, N.C., Hilker,  
1259 T., Bater, C.W., Gobakken, T. (2012). Lidar sampling for large-area forest  
1260 characterization: A review. *Remote Sensing of Environment*. 121, 196–209.  
1261 <https://doi.org/10.1016/j.rse.2012.02.001>
- 1262 Xiao, J., Chevallier, F., Gomez, C., Guanter, L., Hicke, J.A., Huete, A.R., Ichii, K., Ni,  
1263 W., Pang, Y., Rahman, A.F., Sun, G., Yuan, W., Zhang, L., Zhang, X. (2019) Remote  
1264 sensing of the terrestrial carbon cycle: A review of advances over 50 years. *Remote*  
1265 *Sensing of Environment*, 233, 111383. <https://doi.org/10.1016/j.rse.2019.111383>.
- 1266 Yang, W., Ni-Meister, W., & Lee, S. (2011). Assessment of the impacts of surface  
1267 topography, off-nadir pointing and vegetation structure on vegetation lidar  
1268 waveforms using an extended geometric optical and radiative transfer model. *Remote*  
1269 *Sensing of Environment*, 115(11), 2810-2822. <https://doi.org/10.1016/j.rse.2010.02.021>
- 1270 Zanne, A., Lopez-Gonzalez, G Coomes, D., Ilic, J., Jansen, S., Lewis, S., Miller, R.,  
1271 Swenson, N., Wiemann, M., & Chave, J. 2009. Data from: Towards a worldwide  
1272 wood economics spectrum. Dryad Digital Repository  
1273 <https://doi.org/10.5061/dryad.234>.
- 1274 Zwally, H. J., Schutz, B., Abdalati, W., Abshire, J., Bentley, C., Brenner, A., ... &  
1275 Thomas, R. (2002). ICESat's laser measurements of polar ice, atmosphere, ocean, and  
1276 land. *Journal of Geodynamics*, 34(3-4), 405-445. [https://doi.org/10.1016/S0264-](https://doi.org/10.1016/S0264-3707(02)00042-X)  
1277 [3707\(02\)00042-X](https://doi.org/10.1016/S0264-3707(02)00042-X)
- 1278